water MDPI

Article

Large Eddy Simulations of Flow Past Circular Cylinders to Determine Head Loss Coefficients of Circular Bar Trash Racks with Perpendicular Inflow Conditions

Hannes Zöschg

Unit of Hydraulic Engineering, Department of Infrastructure, University of Innsbruck, 6020 Innsbruck, Austria; hannes.zoeschg@uibk.ac.at

Abstract: Trash racks installed at hydropower plants cause head losses that reduce energy output. Previous research has thoroughly investigated head losses through both experimental and field studies. However, only a limited number of numerical studies have been performed, which have shown significant simplifications in terms of model complexity. In this study, the head loss coefficients ξ of circular bar trash racks (CBTRs) were analyzed using 3D Large Eddy Simulation (LES). Specifically, a single submerged bar oriented perpendicular to the flow direction was studied under homogeneous inflow conditions while (i) the blocking ratio P was varied between 0.043 and 0.444, and (ii) the flow velocity U was varied between 0.3 and 1.0 m/s. The model parameters were selected primarily based on the extensive literature on flow past circular cylinders, particularly at a Reynolds bar number Re_b of 3900. To ensure the validity of the parameters, systematic independence tests were performed, including simulations with three and five bars in the computational domain. The results confirmed the suitability of 3D LES as an appropriate tool to determine ξ of CBTRs. In general, ξ decreased continuously with decreasing P and increased with increasing U when $Re_b \geq 3981$, which is consistent with comparable flow parameters observed in previous studies of flow past circular cylinders. Notably, the study found that the empirical formulas used for comparison tended to underestimate ξ when P was relatively low. Finally, the potential of the presented approach for future applications was discussed in detail.

Keywords: 3D numerical modeling; Computational Fluid Dynamics (CFD); circular bar trash racks; flow past a cylinder; head loss; hydraulics; hydropower plants; Large Eddy Simulation; trash racks

check for updates

Citation: Zöschg, H. Large Eddy Simulations of Flow Past Circular Cylinders to Determine Head Loss Coefficients of Circular Bar Trash Racks with Perpendicular Inflow Conditions. *Water* **2024**, *16*, 347. https://doi.org/10.3390/w16020347

Academic Editors: Helena M. Ramos, Juan Antonio Rodríguez Díaz and Jorge Matos

Received: 22 December 2023
Revised: 11 January 2024
Accepted: 16 January 2024
Published: 20 January 2024

Copyright: © 2024 by the author. Licensee MDPI, Basel, Switzerland. This article is an open access article distributed under the terms and conditions of the Creative Commons Attribution (CC BY) license (https://creativecommons.org/licenses/by/4.0/).

1. Introduction

As essential components of hydropower plants (HPPs), trash racks located upstream of turbine intakes primarily serve to protect turbines and other electromechanical equipment from solids transported by the river, particularly floating debris, driftwood, ice drift, and bedload transport [1–3]. These materials can accumulate on trash racks and cause partial or complete blockage or clogging of the intakes, with potential adverse effects including increased static and dynamic loads [3,4], increased upstream flooding potential [5,6], and reduced energy production [7,8]. Generally, such conventional trash racks consist of an array of horizontally or vertically arranged bars held together by support structures. Rack cleaning machines are commonly used to remove accumulated debris. Values for the clear bar spacing b of conventional trash racks typically range from about 20 to 300 mm [2]. By reducing b, trash racks can also serve to protect fish during their downstream migration, as the majority of fish cannot physically pass the rack due to their body proportions [9,10]. Consequently, they cannot enter the turbines, which is associated with a high risk of injury or mortality due to direct contact with blades or other turbine structures, sudden pressure changes, or increased shear or turbulence [11,12]. Typical b values of physical barriers for fish protection range from 10 to 30 mm [10,13], with the recommendation that b should be determined based on the size of the target fish species in the particular river section [14,15]. Another type of barrier that can be used for fish protection is the behavioral barrier, which uses external stimuli such as electricity, light, sound, or the creation of turbulent currents to elicit an avoidance or escape response in fish [16–18]. More recently, hybrid barriers have been increasingly studied, which combine conventional racks or racks for fish protection with an electric field to add an additional behavioral effect to an existing or newly constructed rack [19–23]. Hybrid barriers offer a distinct advantage over racks which provide only a physical barrier effect, allowing the use of larger b values, while still effectively protecting fish [19,20].

When a trash rack is installed upstream of an HPP, some of the kinetic energy of the water is converted into heat as it flows through the rack, which can be considered a loss to the mechanical system and is therefore referred to as an energy or hydraulic loss [2]. These losses are mainly influenced by the geometry of the rack and its arrangement relative to the flow direction, as well as the flow conditions [2]. In practical applications, such as the design phase of a trash rack at an HPP, hydraulic losses are typically calculated using empirical formulas derived from experimental models or empirical data sets. Kirschmer [24] was one of the first to conduct experiments with metal and wooden racks with vertical bars in a flume, varying key parameters such as b, the bar thickness s, and the rack angle relative to the ground plane β. In addition, different bar cross-sectional shapes were investigated, including circular bar trash racks (CBTRs). To determine the head loss coefficient ξ of the studied racks, Kirschmer [24] proposed the formula

$$\xi = k_F \left(\frac{s}{b}\right)^{\frac{4}{3}} \sin\beta, \tag{1}$$

where k_F is the bar shape coefficient. Since then, many researchers have conducted experiments to assess the hydraulic losses of trash racks by analyzing the effect of unit discharge q, flow velocity U, rack angle relative to the side wall α, bar orientation (horizontal or vertical), and other parameters beyond those studied by Kirschmer [24] that affect ξ [2,12,15,25–35]. For example, Meusburger [2] extended Kirschmer's [24] formula by including the area of spacers and support structures along with the area of the bars through the blocking ratio P. Furthermore, the influence of sectional clogging of the rack, expressed by the loss factor k_V, and the horizontal inflow angle to the rack δ, defined as $\delta = 90^\circ - \alpha$ for undisturbed homogeneous flow conditions upstream of the rack, were also considered. The formula proposed by Meusburger [2] can be expressed as

$$\xi = k_F \left(\frac{P}{1-P}\right)^{\frac{3}{2}} \left(1 - \frac{\delta}{90^\circ}\right) P^{-1.4\tan\delta} k_V \sin\beta. \tag{2}$$

Although the experiments were limited to rectangular bars, other bar shapes such as CBTRs can be considered using the k_F values given by Kirschmer [24] in Equation (2) [2]. Böttcher et al. [29] conducted experiments in a flume using horizontally oriented CBTRs and flexible steel cables. Based on the results, an adapted version of Equation (2) was proposed for both rack options, which for CBTRs is given by

$$\xi = 1.80 \left(\frac{P}{1-P}\right)^{1.3} (\sin\alpha)^{1.7}. \tag{3}$$

Further empirical formulas for determining ξ of CBTRs have been proposed by Josiah et al. [27], Zayed et al. [28,36], Spangler [37], Berezinski [38], and the United States Army Corps of Engineers (USACE) [39]. In addition, other researchers, including Tsikata et al. [12], Fellenius and Lindquist [40], Escande [41], Orsborn [42], Zimmermann [43], the Bureau of Reclamation [44], and Clark et al. [45], have suggested formulas for conventional racks with non-circular bar shapes based on physical model experiments, field studies, and empirical data sets. Likewise, formulas for fish protection racks have been proposed by Albayrak et al. [15,46], Raynal et al. [25,26], Beck et al. [30], and Meister et al. [32], among others.

Advances in computational power and the growth of high-performance computing (HPC) clusters have made numerical simulations an important tool for studying hydraulic problems over the last decades. However, studies investigating ξ of trash racks have been limited to a small number of cases [12,31,34], using significant simplifications in terms of model complexity. For example, Raynal et al. [47] performed 2D numerical simulations of angled bar racks by solving the Reynolds-averaged Navier–Stokes (RANS) equations and compared the results with data from previous physical model tests [26,48]. The study found that the ξ values obtained from the numerical simulations were at least 7% lower than those obtained from the physical model. The discrepancies were attributed to the lack of spacers and the inability to replicate 3D effects in 2D simulations. Similarly, Åkerstedt et al. [49] and Leuch et al. [50] used comparable approaches and showed mostly divergent results for ξ when compared to physical model tests. In the former study, the discrepancies were related to the absence of 3D effects, as already noted by Raynal et al. [47], and the application of the RANS approach. The authors recommended that future research should implement more sophisticated models, such as Large Eddy Simulation (LES). Lučin et al. [31] performed 2D and 3D simulations of vertically arranged angled bar racks using the RANS approach based on the physical models of Albayrak et al. [46]. The study found that ξ was underestimated by about 15% compared to the physical model tests, while the 2D and 3D simulations produced comparable ξ values. Again, the use of LES was suggested for future research rather than the RANS approach, which relies on mean flow characteristics [51]. LES, on the other hand, applies a spatial filtering technique to resolve large-scale eddies, while smaller eddies are accounted for using a subgrid-scale (SGS) turbulence transport model [51–53]. By incorporating large turbulent parameters into the numerical solver, LES generally achieves higher accuracy. However, a finer mesh discretization is required [51], resulting in a higher computational cost. To reduce the computational cost, the number of mesh elements can be reduced by focusing on a limited number of bars within the numerical domain. For example, Nascimento et al. [54] performed simulations using the LES model with only two rectangular bars in a 2D domain to investigate the vortex shedding frequencies induced by the rack, but they excluded ξ in the analysis. Other researchers, including Ghamry and Katopodis [55], Paul and Adaramola [56], Jeethulakshmi et al. [57], and Čarija et al. [58], also performed simulations with the number of bars n ranging from 1 to 14, mainly using the RANS approach and 3D domains, and calculated ξ. Typically, the results overestimated ξ compared to the values derived from empirical formulas and previous model tests. Recently, Latif et al. [34] performed 3D RANS simulations of three rectangular bars and proposed a prediction formula for ξ as a function of b, P, and β based on the results. The obtained values were in good agreement with ξ measured at a real HPP, but tended to overestimate the calculated ξ values of empirical formulas, including Kirschmer [24].

Although, to the best of the author's knowledge, no simulations of resolved bars in a 3D domain have been performed using the LES model to determine ξ of trash racks, it has been widely used in other engineering applications, such as flows around bridge piers [59], ground vehicles [60], and high-rise buildings [61]. Many of these studies are mainly based on a classical fluid mechanics problem, the flow past a bluff body, in particular a circular cylinder [62]. Flows in the subcritical regime with bar Reynolds numbers

$$Re_b = \frac{U_{ref}\, s}{\nu}, \tag{4}$$

where U_{ref} is the free-stream velocity, and ν is the kinematic viscosity, ranging from 300 to 140,000 [63], are of significant interest due to the complexity around the cylinder wake [64] with the transition from laminar to turbulent within the separated shear layer [65–67]. Specifically, the flow around a circular cylinder at Re_b = 3900 has been extensively studied through a variety of experimental and numerical methods (e.g., [66,68–72]). Besides LES, researchers have also used Direct Numerical Simulation (DNS, e.g., [73–75]) and Detached Eddy Simulation (DES, e.g., [76,77]). The former method is known to provide the most accurate and reliable results, but requires relatively high computational effort even at low

Re_b [51,64]. The latter method combines the RANS and LES methods by applying the RANS approach in the near-wall region and the LES model in the distant flow regions [52,53,77]. In general, the results of the aforementioned studies using LES, DNS, and DES were found to be in good agreement with experimental studies. Conversely, the use of the RANS method or the unsteady RANS (URANS) method showed larger discrepancies with experimental data in previous studies (e.g., [76,78]). These results suggest that the URANS approach is not capable of accurately predicting the transient flow characteristics of flow past a bluff body [79,80]. Furthermore, previous studies have shown that 2D numerical simulations provide inaccurate values for most flow parameters when $Re_b \geq 250$ [66,67,81]. Therefore, to account for the 3D wake instabilities in the subcritical regime and to obtain accurate results, 3D numerical simulations are recommended [66,82]. In addition to the flow past a single cylinder, the literature contains numerous studies of the flow past two or more circular cylinders arranged in various tandem, side-by-side, or staggered patterns [83,84]. The relevant flow parameters in these cases are mainly influenced by b and Re_b [83–85]. Finally, several studies have investigated the flow past a circular cylinder placed between two parallel walls [86]. Small wall distances can significantly affect the periodic vortex shedding behind the cylinder, as well as other flow structures, indicating that the flow parameters of a confined compared to an unconfined cylinder can vary strongly as a function of P [86–88].

In the present study, 3D numerical simulations using the LES model were performed for a single bar and three or five bars of CBTRs arranged in a side-by-side pattern to determine ξ, mainly based on recommendations from previous research on flow past one or more circular cylinders in confined or unconfined channels and preliminary simulations. The resulting data were then compared with previous studies. The objective of the study was to evaluate the applicability of the presented approach in determining ξ of CBTRs with perpendicular inflow conditions. Furthermore, the effects of b and U on ξ of CBTRs were investigated.

2. Materials and Methods

2.1. Overview and Test Cases

The commercial Computational Fluid Dynamics (CFD) code ANSYS Fluent 19.2 was used for the present study. In order to reduce the high computational cost of the numerical simulations, this study focused on investigating relatively short sections of single bars or arrays of three or five bars of CBTRs in a flume, as schematically shown in Figure 1. The inflow conditions to these sections were idealized (i.e., ideally homogeneous and perpendicular with $\alpha = 90°$ and $\beta = 90°$, no clogging, and no rack damage). The rack sections were fully submerged in water to avoid free surface effects and positioned away from walls to avoid friction effects. For these reasons, as well as for the selected boundary conditions described in Section 2.2, the investigated sections are independent of the orientation of the bars. Horizontally oriented bars are considered in the following, although the results are also applicable to vertically oriented bars.

The rack configurations investigated were inspired by physical models from previous studies, in particular, Böttcher et al. [29] and Meister et al. [32]. The dimensions were approximately in the prototype range (scale 1:1), with $s = 8$ mm and $b = 10$, 20, and 30 mm. These b values were investigated in computational domains with $n = 1$, 3, and 5 bars. Larger values of b, ranging from 40 to 120 mm in increments of 10 mm, as well as 150 mm and 180 mm, were also investigated, but only for the case of a single bar, since the total number of elements in the computational domain N_t increases linearly with n. Instead, additional simulations were performed with periodic boundary conditions at the top and bottom of the computational domains to investigate a similar effect (see Section 2.2). Since the present study did not consider spacers or other support structures, the ratio of the blocked area to the total rack area was calculated as $P = s/(s + b)$. Consequently, P ranged from 0.043 (for $b = 180$ mm) to 0.444 (for $b = 10$ mm). Furthermore, the effect of U on ξ was investigated by varying the flow velocity at the inlet of the computational domain U_1 from

0.3 to 1.0 m/s in steps of 0.1 m/s for a single bar with b values of 10, 20, and 30 mm. The lower limit of U_1 was set at 0.3 m/s (corresponding to Re_b = 2389) to avoid perturbations caused by undersized computational domains, as reported by Jiang and Cheng [89] for flow past a circular cylinder at $Re_b \leq 2000$. To keep critical computational parameters that could affect the results within an acceptable range, the upper limit of U_1 was set at 1.0 m/s (corresponding to Re_b = 7962). In addition, to investigate the effect of U_1 in a setting where the influence of the top and bottom walls of the computational domain is negligible, U_1 was also varied for a case with a larger b value. For this purpose, b = 90 mm was chosen, resulting in P = 0.082, which is less than 0.100 as recommended by Norberg [90] to avoid top and bottom wall effects.

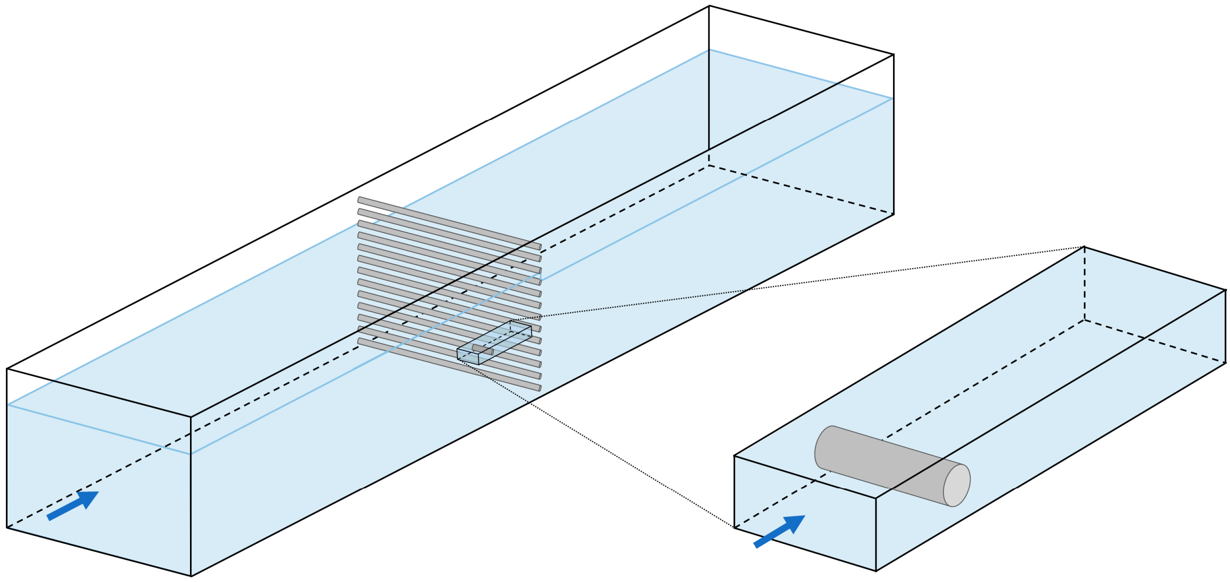

(**a**) (**b**)

Figure 1. Schematics of (**a**) a complete model of a horizontally arranged circular bar trash rack (CBTR) in a flume, and (**b**) a waterbody segment consisting of a single bar section taken from (**a**): Such segments served as the basis for defining the computational domains in this study. The arrows indicate the direction of flow.

In this study, water density ρ was defined as 998.2 kg/m^3 at a constant temperature of 20 °C, and ν was defined as 0.0000010048 m^2/s. When U_{ref} or U_1 (interchangeable terms in this study) is equal to 0.5 m/s, Equation (4) calculates Re_b to be 3981. This value is close to the frequently used Re_b value of 3900 in previous research on flow past a circular cylinder, as noted in Section 1. Due to the similarities between the present problem and this classic topic, along with the large amount of data available for Re_b = 3900, the basic settings and recommendations for the numerical simulations in this study were adopted. To assess the appropriateness of these settings and recommendations for the determination of ξ, systematic independence tests were performed for the single-bar case with the lowest b value of 10 mm or the highest P of 0.444 at Re_b = 3981, as well as in selected cases with b = 90 mm (P = 0.082).

2.2. Computational Domains and Boundary Conditions

Hexahedral domains in a Cartesian coordinate system were used for the simulations in this study. The x, y, and z axes represented the streamwise, spanwise, and vertical directions, respectively. In the case of a single bar, the bar was placed symmetrically between two parallel walls in the vertical direction, each equidistant from the boundaries by $b/2$. Figure 2 shows a schematic representation of such a computational domain. In the cases where n = 3 and 5 were used, the equivalent number of single-bar domains were superimposed, with b as the distance between two bars. The dimensions of the domains in the streamwise, spanwise, and vertical directions are denoted as L_x, L_y, and L_z, respectively. L_x can be further divided into upstream and downstream parts separated by the examined rack section (i.e., $L_x = L_{x,us} + s + L_{x,ds}$). $L_{x,ds}$, $L_{x,us}$, and L_y were initially defined based on the literature data and preliminary simulations. These lengths were then validated in the independence test using the lengths given in Section 3.1.2. In contrast, the value of L_z is a function of the chosen values of n and P, described as $L_z = n\ (s + b)$.

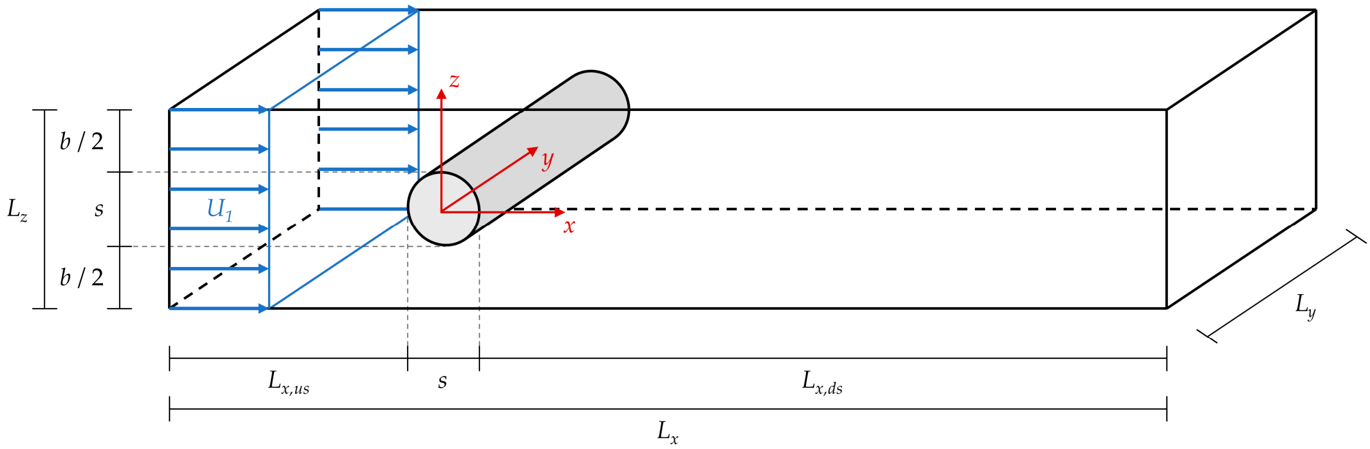

Figure 2. Schematic of a computational domain with a single bar, where b is the clear bar spacing, L_x, L_y, and L_z are the lengths of the domain in the streamwise, spanwise, and vertical directions, respectively, $L_{x,ds}$ and $L_{x,us}$ are the lengths of the domain downstream and upstream of the bar, respectively, in the streamwise direction, s is the bar thickness, and U_1 is the flow velocity at the inlet.

At the inlet of the domains, the velocity inlet boundary condition was used with a constant value of U_1. At the outlet, the pressure outlet boundary condition was applied with zero static gauge pressure. Periodic boundary conditions were used in the spanwise direction to assume an infinite length of the bars, as often used in previous studies of flow past circular cylinders (e.g., [69,85,88]), thereby reducing the end wall effects on the three-dimensional flow conditions. Unlike most studies of flow past a confined cylinder (e.g., [88,91]), which used no-slip wall boundary conditions for the top and bottom of the computational domains, this study mainly used free-slip wall boundary conditions. The application of free-slip wall and periodic boundary conditions in the vertical and spanwise directions, respectively, resulted in no frictional losses along the walls, thus producing a uniform velocity profile with U_1 across the cross section far upstream of the rack section, as shown in Figure 2. The surfaces of the bars were subjected to a no-slip wall condition to represent the velocity gradient, which is zero at the surfaces and reaches free-flow velocity at a sufficient distance from the bars. It should also be noted that periodic top and bottom boundary conditions were used for a limited number of simulations, as described in Section 2.1.

2.3. Spatial and Temporal Discretization

Following the methodology used in several previous studies of flow past a cylinder [64], a hybrid mesh was used as the mesh pattern, consisting of an O-grid in the near-field grid around each bar and an H-grid in the outer regions. An example of the mesh structure in the x–z plane is shown in Figure 3, which shows the front part of a computational domain with $n = 3$ and the surface of one of the bars in detail. The near-field grid of each bar consisted of a concentric ring shape with an outer diameter of $2s$ starting from the center of each bar. This size was chosen to ensure homogeneity in the near-field grid construction across all simulations, regardless of L_z. In the near-field grid, the resolution in the x–z plane was defined by the number of elements on the bar circumference and in the radial direction, denoted as N_c and N_r, respectively. To resolve the viscous sublayer of the near-wall region, the dimensionless distance from the wall y^+ should be less than one. To achieve this, the height of the first cell adjacent to the bars was set to about 0.00001 m, or about 0.00125s in all simulations. The grid resolution was then increased radially based on N_r. In the outer regions, a maximum grid stretch ratio based on the ratio in the near-field grid was used. By applying periodic and free-slip conditions in the spanwise and vertical directions, respectively, no refined grid resolution was required near the outer boundaries of the domains. In contrast to the x–z plane, the mesh was uniformly structured in the spanwise direction, i.e., the mesh generated in the streamwise and vertical directions was extruded in the spanwise direction with uniform resolution L_y/N_y, where N_y is the number of elements in the spanwise direction. The effects of varying N_c, N_r, and N_y on the results were evaluated in the independence test described in Section 3.1.3. In addition, N_t is reported for all simulations in Section 3.1.

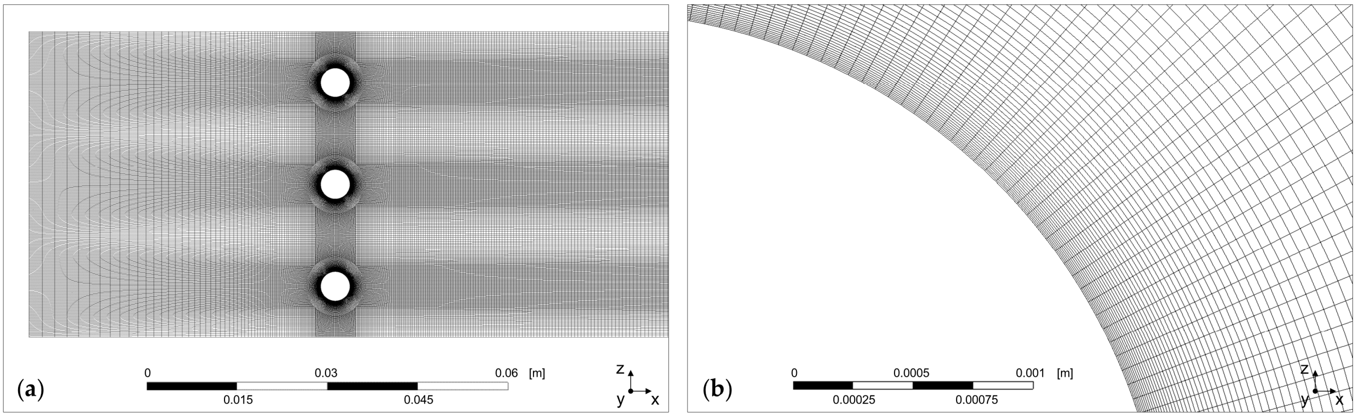

Figure 3. Computational mesh of a simulation consisting of three bars with a clear bar spacing of b = 20 mm and a domain length in the streamwise direction of L_x = 111s in the x–z plane: (**a**) overview of the front part of the domain, and (**b**) close-up view of the surface of one of the bars.

As a second criterion to evaluate the quality of the meshes, the LES index of quality LES_{IQ} was used, which is defined as the ratio of the resolved turbulent kinetic energy k_r to the total turbulent kinetic energy k_t, and is calculated as

$$LES_{IQ} = \frac{k_r}{k_t} = \frac{1}{1 + 0.05\left(\frac{\nu+\nu_{sgs}}{\nu}\right)^{0.53}}, \quad (5)$$

where ν_{sgs} is the SGS eddy viscosity (see Section 2.4). According to Celik et al. [92], LES_{IQ} values in the range of 75% to 85% are appropriate for most engineering applications. Pope [51] recommends a percentage of k_r above 80% for well-resolved LES.

All simulations in this study used a fixed time step Δt. The effect of Δt on the results was evaluated in the independence test described in Section 3.1.4. Furthermore, the total simulation time was defined based on the evaluation time t_e for relevant flow parameters and is therefore explained in Section 2.5.

2.4. Numerical Methods

The 3D numerical simulations in this study use the incompressible form of the Navier–Stokes equations (i.e., ρ is constant). The LES model relies on the filtered form of the continuity and momentum equations, obtained by a filter operation and expressed as

$$\frac{\partial \overline{u}_i}{\partial x_i} = 0, \quad (6)$$

$$\frac{\partial \overline{u}_i}{\partial t} + \frac{\partial \overline{u_i u_j}}{\partial x_j} = -\frac{1}{\rho}\frac{\partial \overline{p}}{\partial x_i} + \nu\frac{\partial^2 \overline{u}_i}{\partial x_i \partial x_j} - \frac{\partial \tau_{ij}}{\partial x_i}, \quad (7)$$

where u_i are the flow velocity components, x_i are the Cartesian coordinates, t is the time, and p is the pressure. In addition, the macron denotes the grid-scale filter operation, and τ_{ij} represents the SGS stress tensor, defined as

$$\tau_{ij} = \overline{u_i u_j} - \overline{u}_i \overline{u}_j. \tag{8}$$

Modeling is required to account for the unknown SGS stresses [51]. The Smagorinsky SGS model [93] was used in this study for this purpose, which calculates the SGS turbulent stresses as

$$\tau_{ij} - \frac{1}{3}\tau_{kk}\delta_{ij} = -2\nu_{sgs}\overline{S}_{ij}, \tag{9}$$

where δ_{ij} is the Kronecker delta symbol, and S_{ij} is the resolved rate of the strain tensor. ν_{sgs} is defined as

$$\nu_{sgs} = \left(C_s\overline{\Delta}\right)^2 \left|\overline{S}\right|, \tag{10}$$

where C_s is the Smagorinsky coefficient, Δ is the grid size defining the subgrid length scale, and $|S|$ is the characteristic filtered rate of strain. In ANSYS Fluent 19.2, C_s can be defined either by a constant value (hereafter referred to as the Smagorinsky–Lilly model) or dynamically based on data obtained from the resolved motion scales (hereafter referred to as the dynamic Smagorinsky–Lilly model) [94]. Previous studies have shown that the latter is more accurate in predicting flow parameters for flow past a cylinder (e.g., [66,69]). Therefore, the dynamic model was primarily used in this study. Nevertheless, in Section 3.1.6, results using the Smagorinsky–Lilly model with a fixed C_s value of 0.1, which is the default value in ANSYS Fluent 19.2 [94], were compared with those using dynamic C_s values. In addition, simulations using the URANS approach and the hybrid model DES were performed to evaluate their ability to predict ξ and other flow parameters in a manner comparable to LES. The Shear Stress Transport (SST) k-ω model proposed by Menter [95] was used to model turbulence for both the DES model and the URANS approach. Since these two methods are only used for comparison in the present work, the governing equations are not included here, but can be found in the literature [51,94], along with additional information on the LES model.

In all numerical simulations, the Semi-Implicit Method for Pressure-Linked Equations (SIMPLE) algorithm was used for the pressure–velocity coupling, which has previously been used in studies to determine ξ (e.g., [31,57]) and to study flow past a cylinder (e.g., [64,80]). Specifically, in the LES model, Equations (6) and (7) are solved using the SIMPLE algorithm. Furthermore, the LES and DES models used bounded central differencing and bounded second-order implicit schemes for spatial discretization and transient formulation, respectively. In contrast, the URANS simulations used second-order upwind and second-order implicit schemes for spatial discretization and transient formulation, respectively.

The numerical simulations were performed on the LEO HPC infrastructure of the University of Innsbruck with 64 cores each. To avoid rounding errors, all simulations were performed in double precision.

2.5. Post-Processing

After performing the numerical simulations, the results were subjected to a thorough error check, including visual inspection of the velocity and pressure profiles and distributions along with other numerical results. MATLAB R2018b software was used for further analysis of the results, except for the determination of the Strouhal number St, which was performed using ANSYS Fluent 19.2.

The calculation of ξ was determined using the Bernoulli equation with the cross-sectional averaged parameters at the inlet (subscript 1) and outlet (subscript 2) of the domain. Due to the chosen boundary conditions, there were no frictional losses at the domain boundaries and thus no continuous head losses between the cross sections. Consequently, the local head loss h_v is equal to the total head loss, and can be calculated as

$$h_v = z_1 - z_2 + \frac{p_1 - p_2}{\rho\, g} + \frac{\alpha_{kin,1}\, U_1^2 - \alpha_{kin,2}\, U_2^2}{2g} = \xi \frac{U_{ref}^2}{2g}, \tag{11}$$

where z_1 and z_2 are the elevations, g is the gravitational acceleration, and $\alpha_{kin,1}$ and $\alpha_{kin,2}$ are the kinetic energy correction factors. In previous studies (e.g., [2,29,32]), U_{ref} was defined as the undisturbed cross-sectional average flow velocity upstream of the rack, assuming that the velocities upstream and downstream of the rack do not differ significantly. In this study, this approach is adopted due to the defined computational domains and boundary conditions described in Section 2.2, which imply that U_1 is equal to U_{ref} and, except for non-uniformities in the velocity profile, is also equal to U_2. To account for non-uniformities in the respective cross sections, α_{kin} was used. In general, α_{kin} is defined as the ratio of the kinetic energies between the actual velocity profile and the theoretical profile with constant mean flow velocity $\overline{U}$ over the cross-sectional area A [96,97], and is calculated as

$$\alpha_{kin} = \frac{1}{\overline{U}^3\, A} \int_A U^3(A) dA. \tag{12}$$

Typical values of α_{kin} in a pipe range from 1.00 for turbulent velocity distributions with a uniform constant velocity profile to 2.00 for laminar conditions with a parabolic profile [97–99]. Previous studies have generally ignored the effect of α_{kin} on ξ due to its relatively low values close to unity, such as between 1.01 and 1.02 in Tsikata et al. [12]. In the simulations of the present study, $\alpha_{kin,1}$ was exactly unity (excluding rounding errors) due to the ideal homogeneous flow field at the inlet. Conversely, $\alpha_{kin,2}$ ranged between 1.001 and 1.011, as shown in the domain independence test in Section 3.1.2. Therefore, α_{kin} was not included in the calculation of ξ. Furthermore, the inlet and outlet of the water body segments were assumed to be at the same height (i.e., $z_1 = z_2$). For p_1 and p_2, the cross-sectional averaged total pressure at the inlet and outlet were used, respectively. Considering all these factors, Equation (11) can be expressed as

$$\xi = \frac{2(p_1 - p_2)}{\rho\, U_1^2}. \tag{13}$$

In addition to Equation (13), ξ can also be determined using the drag coefficient C_D and P [2,99] by

$$\xi = C_D\, P. \tag{14}$$

C_D is a parameter often studied in the analysis of flow past a cylinder [63,86] and is defined as

$$C_D = \frac{F_D}{0.5 U_1^2\, s\, L_y}, \tag{15}$$

where F_D is the drag force. Another commonly studied flow parameter is St, which is a dimensionless number that characterizes the shedding frequency independent of time. St can be calculated as

$$St = \frac{f_v s}{U_1}, \tag{16}$$

where f_v is the vortex shedding frequency determined by calculating the frequency corresponding to the maximum energy of the spectra obtained by a Fast Fourier Transform (FFT) of the time series of the lift coefficient C_L, which is defined as

$$C_L = \frac{F_L}{0.5 U_1^2\, s\, L_y}, \tag{17}$$

where F_L is the lift force on the cylinder. Both C_D and St were calculated for all simulations in this study to allow comparison with previous research on flow past a cylinder.

In post-processing, the collected data from each time step were averaged using the mean value over a specified period after an initial period, which was necessary to ensure that the flow was statistically quasi-steady and to remove initial transients. In previous studies, these periods were usually defined based on a certain number of vortex shedding cycles $T = 1/f_v$ (e.g., [70,71]). Due to significant variations in St ranging from 0.208 to 0.340, as observed in the simulations of this study (see Section 3), standardized values were used to define the critical periods, with $St = 0.200$ and $U_1 = 0.5$ m/s. The former is a typical value for flow past an unconfined cylinder in the subcritical regime [63] and is lower than the minimum St value obtained in this study. Consequently, the data averaging period was set to a minimum of 100T, resulting in $t_e = 8$ s according to Equation (16), after an initial period of 50T, which is equivalent to 4 s. The total simulation time was 12 s, except for simulations where $U_1 < 0.5$ m/s. In these cases, the total simulation time, including t_e, was extended to maintain a consistent minimum number of T across all simulations. Notably, the use of the same time period for different P values, rather than adjusting the data averaging period to f_v, is consistent with previous experimental studies aimed at determining ξ (e.g., [29,32]). Furthermore, the effect of extending t_e was examined in the independence test described in Section 3.1.4.

Finally, it is important to clarify that the parameters obtained from the numerical calculations presented in the following sections, such as ξ and C_D, represent time–mean values. For values that fluctuate over time, additional subscripts are added to denote them, such as ξ_f and C_{Df}. In addition, Equation (13) was used to calculate ξ unless otherwise noted.

3. Results

3.1. Independence Tests

3.1.1. General

Independence tests are critical when performing time-consuming and computationally expensive numerical simulations to evaluate the effects of selected model settings on the results. For the independence tests in this study, the reference case parameters listed in Table 1 were used, with U_1 held constant at 0.5 m/s (corresponding to $Re_b = 3981$). Unless otherwise specified, $b = 10$ mm ($P = 0.444$) was used. The parameters in Table 1 were then individually adjusted to evaluate their effect on ξ, C_D, St, and other key parameters through a sensitivity analysis. To quantify the differences, the mean relative error (MRE), defined as the ratio of the mean absolute error to the mean reference value, was calculated for ξ and C_D. It should be noted that key parameters such as ξ and C_D are susceptible to time-dependent fluctuations (see Section 3.1.4). In order to assess the influence of these fluctuations on the results, selected simulations with different values of b were repeated. As a result, the time–mean values for both ξ and C_D showed minimal differences, except for a maximum MRE of 1.4% in one simulation. Therefore, 1.4% was used as a threshold for an acceptable range of MRE in the following.

Table 1. Selected values for the parameters of the reference case and the selected reference LES model in the independence tests, independent of the studied clear bar spacings b, where $L_{x,ds}$ and $L_{x,ds}$ are the lengths of the domain downstream and upstream of the studied rack section, respectively, in the streamwise direction, L_y is the length of the domain in the spanwise direction, n is the number of bars in the domain, N_c, N_r, and N_y are the number of elements in the bar circumference, the radial direction of the near-field grid, and the spanwise direction, respectively, t_e is the evaluation time, and Δt is the time step.

$L_{x,us}$ [-]	$L_{x,ds}$ [-]	L_y [-]	n [-]	N_c [-]	N_r [-]	N_y [-]	t_e [s]	Δt [s]	LES Model
10s	100s	4s	1	240	64	80	8	0.00004	Dynamic Smagorinsky–Lilly

3.1.2. Domain Independence

Defining sufficiently large domains is essential to reduce potential influences from both domain size and boundary conditions, which is particularly important for L_x and L_y in this study. Table 2 shows the results of the domain independence test for the determination of ξ, C_D, St, and $\alpha_{kin,2}$. Doubling the reference case value of $L_{x,us}$ resulted in insignificant changes in the results (−0.3% for ξ and −0.4% for C_D), indicating that $L_{x,us}$ = 10s is sufficient to establish homogeneous inflow conditions to the studied rack section. Similarly, $L_{x,ds}$ must be sufficient to provide uniform flow conditions at the outlet without significant recirculation zones. Halving and doubling $L_{x,ds}$ resulted in negligible effects (−0.9% and +0.3%, respectively) on both ξ and C_D. However, when $L_{x,ds}$ was set to 50s, small recirculation zones were observed at the outlet, resulting in a higher value of $\alpha_{kin,2}$ compared to the reference case. Nevertheless, $\alpha_{kin,2}$ = 1.011 is still within an acceptable range as described in Section 2.5. Furthermore, doubling L_y had no significant effect on the results, but halving L_y increased ξ by 1.9% and C_D by 1.7%. These results suggest that the reference case values have a satisfactory degree of domain independence.

Table 2. Results of the domain independence test to determine the drag coefficient C_D, the Strouhal number St, the kinetic energy correction factor at the outlet $\alpha_{kin,2}$, and the head loss coefficient ξ, calculated using Equation (13), where L_v is used as a variable for the length of the domain upstream and downstream of the studied rack section in the streamwise direction $L_{x,us}$ and $L_{x,ds}$, respectively, and in the spanwise direction L_y. In addition, N_t is the total number of elements in the domain.

Parameter	L_v [-]	N_t [-]	ξ (MRE) [-]	C_D (MRE) [-]	St [-]	$\alpha_{kin,2}$ [-]
$L_{x,us}$	10s	4,312,000	1.262 (Ref.)	2.840 (Ref.)	0.296	1.002
	20s	4,408,320	1.258 (−0.3%)	2.830 (−0.4%)	0.296	1.002
$L_{x,ds}$	50s	3,706,560	1.251 (−0.9%)	2.815 (−0.9%)	0.298	1.011
	100s	4,312,000	1.262 (Ref.)	2.840 (Ref.)	0.296	1.002
	200s	4,697,280	1.266 (+0.3%)	2.848 (+0.3%)	0.296	1.001
L_y	2s	2,156,000	1.285 (+1.9%)	2.889 (+1.7%)	0.294	1.007
	4s	4,312,000	1.262 (Ref.)	2.840 (Ref.)	0.296	1.002
	8s	8,624,000	1.257 (−0.3%)	2.833 (−0.3%)	0.296	1.003

3.1.3. Grid Independence

Table 3 shows the results of the grid independence test for the determination of ξ, C_D, and St. In addition, the volume-averaged mean value of LES_{IQ} and the minimum value of LES_{IQ} over all time steps of t_e, denoted as $LES_{IQ,avg}$ and $LES_{IQ,min}$, respectively, are listed in Table 3. Increasing N_c or N_r had minimal effects on the results, while decreasing them caused changes in ξ and C_D equal to or greater than 1.5%. Thus, the values chosen for N_c and N_r in the reference case appear to be appropriate. It should be noted that N_r = 32, 48, 64, and 80 correspond to mesh growth rates of 1.133, 1.074, 1.048, and 1.034, respectively. Furthermore, Table 3 shows that a large number of simulations were performed with different values of N_y because of its importance for the results, as reported in previous studies (e.g., [64,69]). Halving N_y from 80 to 40 resulted in a 1.3% decrease in both ξ and C_D. Conversely, increasing N_y also resulted in decreased values of ξ and C_D, but to different extents. For N_y = 120 and 160, both ξ and C_D decreased by 0.5% and 2.1%, respectively, compared to the reference case. In addition, for N_y = 240, ξ decreased by 0.9% and C_D decreased by 1.0%. These results indicate that ξ and C_D tend to vary depending on the chosen N_y value, but generally remain close to an average value. Thus, the choice of N_y = 80 as the reference value seems to produce satisfactory results while keeping the computational effort at an acceptable level. Moreover, a simulation with N_y = 1 was performed, which basically corresponds to a simplified 2D case, since 3D vortices cannot occur due to the use of only one element in the spanwise direction. The results showed a 22.4% increase in ξ and a 13.7% increase in C_D compared to the reference case, well above the threshold of acceptable values for the MRE. When LES_{IQ} was used as a complementary metric to evaluate mesh quality, a correlation between LES_{IQ} and mesh resolution was observed, with a significant increase in $LES_{IQ,min}$ as N_y increased. However, only a small number of elements exhibited LES_{IQ} values below the 80% threshold recommended by Pope [51], as detailed in Section 2.3, over the entire t_e. Except for N_y = 1, $LES_{IQ,avg}$ remained approximately constant around 0.948 for all simulations. The results suggest that k_r is in the appropriate range for most simulations. Finally, it is noteworthy that y^+ was consistently less than one for all simulations in the grid independence test.

Table 3. Results of the grid independence test to determine the drag coefficient C_D, the volume-averaged mean value of the LES index of quality $LES_{IQ,avg}$, the minimum value of the LES index of quality over all time steps $LES_{IQ,min}$, the Strouhal number St, and the head loss coefficient ξ, calculated using Equation (13), where N_v is used as a variable for the number of elements on the bar circumference N_c, in the radial direction of the near-field grid N_r, and in the spanwise direction N_y. In addition, N_t is the total number of elements in the domain.

Parameter	N_v [-]	N_t [-]	ξ (MRE) [-]	C_D (MRE) [-]	St [-]	$LES_{IQ,avg}$ [-]	$LES_{IQ,min}$ [-]
N_c	160	3,022,400	1.243 (−1.5%)	2.798 (−1.5%)	0.298	0.947	0.780
	240	4,312,000	1.262 (Ref.)	2.840 (Ref.)	0.296	0.948	0.777
	320	5,614,400	1.262 (±0.0%)	2.839 (±0.0%)	0.296	0.948	0.786
N_r	32	1,824,000	1.304 (+3.3%)	2.935 (+3.3%)	0.292	0.946	0.763
	48	3,254,400	1.280 (+1.5%)	2.882 (+1.5%)	0.294	0.947	0.776
	64	4,312,000	1.262 (Ref.)	2.840 (Ref.)	0.296	0.948	0.777
	80	5,369,600	1.256 (−0.5%)	2.825 (−0.5%)	0.292	0.948	0.794
N_y	1	53,900	1.545 (+22.4%)	3.231 (+13.7%)	0.296	0.919	0.687
	40	2,156,000	1.246 (−1.3%)	2.804 (−1.3%)	0.298	0.946	0.753
	80	4,312,000	1.262 (Ref.)	2.840 (Ref.)	0.296	0.948	0.777
	120	6,468,000	1.256 (−0.5%)	2.827 (−0.5%)	0.292	0.949	0.792
	160	8,624,000	1.236 (−2.1%)	2.782 (−2.1%)	0.300	0.949	0.798
	240	12,936,000	1.250 (−0.9%)	2.813 (−1.0%)	0.298	0.950	0.808

3.1.4. Time Independence

In this study, time independence was tested in two different ways. First, to investigate the influence of the time-dependent fluctuations shown in Figure 4a for ξ_f and C_{Df} on the time–mean results, the total simulation time was extended from 12 to 20 s, thus doubling t_e from 8 to 16 s. Figure 4b shows the time–mean normalized head loss coefficient ξ_n as a function of time for the reference case with b = 10 and 90 mm, while indicating t_e = 8 and 16 s. The calculation of time–mean values started at the beginning of t_e after 4 s of simulation, as defined in Section 2.5. In addition, Table 4 shows the results for the determination of ξ, C_D, and St. When t_e was doubled, both ξ and C_D increased slightly by 0.2% for b = 10 mm (P = 0.444). For b = 90 mm (P = 0.082), the MRE was even smaller for both parameters. Overall, the extension of t_e did not significantly affect the results, indicating that the defined time periods are sufficient to obtain time-independent results at an acceptable level. Second, the reference value of Δt was varied. The results in Table 4 show that halving or doubling Δt had a minimal effect on both ξ and C_D. It is worth noting, however, that instability problems occurred during the simulation with Δt = 0.00008 s. Thus, Δt had to be reduced to 0.00004 s for the first 2 s of the simulation before it was increased to 0.00008 s. The transient instability problems may have been caused by the violation of the Courant–Friedrichs–Lewy condition in some elements, which was not observed in the reference case with Δt = 0.00004 s.

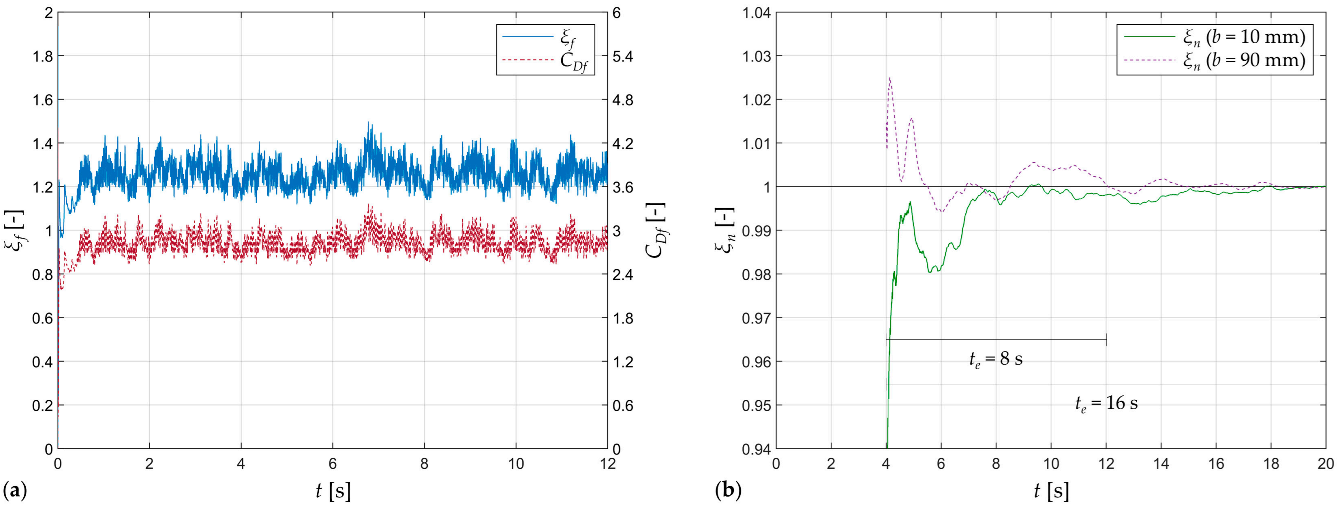

Figure 4. Time histories of (**a**) the fluctuating drag coefficient C_{Df} and the fluctuating head loss coefficient ξ_f for the reference case with clear bar spacing b = 10 mm, and (**b**) the time–mean normalized head loss coefficient ξ_n, starting to compute time–mean values at 4 s, for the reference case values with b = 10 and 90 mm, where t_e are the evaluation times examined as part of the time independence test. ξ_f and ξ_n were calculated using Equation (13).

Table 4. Results of the time independence test to determine the drag coefficient C_D, the Strouhal number St, and the head loss coefficient ξ, calculated using Equation (13), where t_v is used as a variable for the evaluation time t_e and the time step Δt. In addition, b is the clear bar spacing, N_t is the total number of elements in the domain, and P is the blocking ratio.

Parameter	t_v [s]	b [mm]	P [-]	N_t [-]	ξ (MRE) [-]	C_D (MRE) [-]	St [-]
t_e	8 16	10	0.444	4,312,000	1.262 (Ref.) 1.264 (+0.2%)	2.840 (Ref.) 2.845 (+0.2%)	0.296 0.296
	8 16	90	0.082	7,369,600	0.085 (Ref.) 0.085 (±0.0%)	1.026 (Ref.) 1.025 (±0.0%)	0.212 0.215
Δt	0.00002 0.00004 0.00008	10	0.444	4,312,000	1.270 (+0.6%) 1.262 (Ref.) 1.267 (+0.4%)	2.858 (+0.6%) 2.840 (Ref.) 2.850 (+0.4%)	0.300 0.296 0.296

3.1.5. Independence of the Number of Bars in the Computational Domain

Table 5 shows the results of the numerical simulations with b = 10, 20, and 30 mm and n = 3 and 5 for the determination of ξ, C_D, and St compared to those with the corresponding b value and the reference value n = 1. The findings indicate significant single digit percentage differences when n was greater than one. The maximum deviation for both ξ and C_D was 6.0% for b = 20 mm (P = 0.286) and n = 5. As noted in Section 2.1, an increase in n resulted in a corresponding increase in N_t. For example, N_t reached 29,008,000 for b = 30 mm (P = 0.211) and n = 5, as shown in Table 5. Due to the increased N_t values, substantial computational resources were required despite the use of an HPC cluster. Therefore, to facilitate a simplified assessment of the effect of n on the results, additional simulations were performed using periodic boundary conditions at the top and bottom of the domains with n = 1, while b ranged from 10 to 90 mm in 10 mm increments (i.e., P values between 0.082 and 0.444 were examined). The results presented in Table 5 show that the values of ξ and C_D tended to approach the values obtained under free-slip wall conditions as b increased. For b = 10 mm (P = 0.444), the MRE for both ξ and C_D was 15.9%, but decreased to 1.2% for b = 60 mm (P = 0.118), and continued to decrease with increasing b, except for the outlier at b = 90 mm (P = 0.082), which was still within the defined acceptable range of the MRE. Thus, the independence of n was only observed for larger b values. Nevertheless, the feasibility of using the results with $n = 1$ to determine ξ of CBTRs is further discussed in Sections 4.1 and 4.2.

Table 5. Results of the independence test of the number of bars in the computational domain by varying the number of bars n and using different top and bottom boundary conditions to determine the drag coefficient C_D, the Strouhal number St, and the head loss coefficient ξ, calculated using Equation (13), where b is the clear bar spacing, N_t is the total number of elements in the domain, and P is the blocking ratio.

n [-]	Top and Bottom Boundary Condition	b [mm]	P [-]	N_t [-]	ξ (MRE) [-]	C_D (MRE) [-]	St [-]
1	Free-slip wall	10	0.444	4,312,000	1.262 (Ref.)	2.840 (Ref.)	0.296
3	Free-slip wall			12,936,000	1.242 (−1.6%)	2.794 (−1.6%)	0.300
5	Free-slip wall			21,560,000	1.209 (−4.2%)	2.719 (−4.3%)	0.302
1	Periodic			4,312,000	1.061 (−15.9%)	2.390 (−15.9%)	0.340
1	Free-slip wall	20	0.286	5,174,400	0.474 (Ref.)	1.659 (Ref.)	0.244
3	Free-slip wall			15,523,200	0.459 (−3.0%)	1.609 (−3.0%)	0.252
5	Free-slip wall			25,872,000	0.445 (−6.0%)	1.559 (−6.0%)	0.256
1	Periodic			5,174,400	0.409 (−13.6%)	1.434 (−13.6%)	0.276
1	Free-slip wall	30	0.211	5,801,600	0.266 (Ref.)	1.262 (Ref.)	0.240
3	Free-slip wall			17,404,800	0.261 (−1.6%)	1.243 (−1.5%)	0.242
5	Free-slip wall			29,008,000	0.260 (−2.1%)	1.237 (−2.0%)	0.244
1	Periodic			5,801,600	0.256 (−3.8%)	1.216 (−3.7%)	0.246
1	Free-slip wall	40	0.167	6,193,600	0.191 (Ref.)	1.149 (Ref.)	0.230
	Periodic				0.188 (−1.6%)	1.131 (−1.6%)	0.232
1	Free-slip wall	50	0.138	6,507,200	0.150 (Ref.)	1.084 (Ref.)	0.226
	Periodic				0.148 (−1.2%)	1.071 (−1.2%)	0.224
1	Free-slip wall	60	0.118	6,820,800	0.127 (Ref.)	1.068 (Ref.)	0.224
	Periodic				0.125 (−1.2%)	1.057 (−1.1%)	0.222
1	Free-slip wall	70	0.103	7,056,000	0.109 (Ref.)	1.051 (Ref.)	0.216
	Periodic				0.108 (−0.9%)	1.041 (−0.9%)	0.218
1	Free-slip wall	80	0.091	7,212,800	0.095 (Ref.)	1.027 (Ref.)	0.216
	Periodic				0.094 (−0.3%)	1.026 (−0.3%)	0.218
1	Free-slip wall	90	0.082	7,369,600	0.085 (Ref.)	1.026 (Ref.)	0.212
	Periodic				0.084 (−0.8%)	1.018 (−0.8%)	0.216

3.1.6. Method Independence

The results of the comparison with the DES model, the LES Smagorinsky–Lilly model, and the URANS approach are shown in Table 6 for b values of 10 and 90 mm. For b = 10 mm (P = 0.444), the LES Smagorinsky–Lilly model and the URANS approach showed slight differences in ξ and C_D compared to the reference case, with a maximum MRE of −0.8%. Conversely, the DES model produced larger MREs of −4.3%. For b = 90 mm (P = 0.082), the LES (both Smagorinsky–Lilly and dynamic Smagorinsky–Lilly) and DES models yielded comparable results for ξ and C_D with minor differences. However, the URANS simulation produced values that were 23.6% higher for ξ and 23.3% higher for C_D compared to the reference case. The results for b = 90 mm (P = 0.082) were then used to validate the method, which gave results similar to the literature values from previous experimental and numerical studies of flow past a circular cylinder at Re_b = 3900 [64,65,68–72,74,85,89]. The comparison showed that all C_D values were within the literature range of 0.97 to 1.04, except for the value of 1.265 obtained with the URANS approach. In addition, the St values for all simulations were within the literature range of 0.203 to 0.218. Consequently, the results indicate that the reference model with b = 90 mm (P = 0.082) produced comparable values to the literature data for both C_D and St, thereby validating the use of the selected reference case values for simulating flow past a cylinder.

Table 6. Results of the comparison of the DES model, the LES Smagorinsky–Lilly and dynamic Smagorinsky–Lilly models, and the URANS approach to determine the drag coefficient C_D, the Strouhal number St, and the head loss coefficient ξ, calculated using Equation (13), where b is the clear bar spacing, N_t is the total number of elements in the domain, and P is the blocking ratio.

Method	b [mm]	P [-]	N_t [-]	ξ (MRE) [-]	C_D (MRE) [-]	St [-]
DES	10	0.444	4,312,000	1.208 (−4.3%)	2.717 (−4.3%)	0.298
LES (Dynamic Smagorinsky–Lilly)				1.262 (Ref.)	2.840 (Ref.)	0.296
LES (Smagorinsky–Lilly)				1.253 (−0.7%)	2.819 (−0.7%)	0.298
URANS				1.252 (−0.8%)	2.817 (−0.8%)	0.296
DES	90	0.082	7,369,600	0.086 (+0.8%)	1.033 (+0.6%)	0.216
LES (Dynamic Smagorinsky–Lilly)				0.085 (Ref.)	1.026 (Ref.)	0.212
LES (Smagorinsky–Lilly)				0.085 (+0.2%)	1.028 (+0.2%)	0.214
URANS				0.105 (+23.6%)	1.265 (+23.3%)	0.212

3.2. Effect of Clear Bar Spacing or Blocking Ratio

Figure 5 and Table 7 show the effects of varying b or P on ξ and C_D. Increasing b led to a decrease in ξ (Figure 5a), while increasing P led to an increase in ξ (Figure 5b). Similarly, C_D decreased with increasing b or decreasing P, but for b values greater than or equal to 80 mm ($P \leq 0.091$), C_D remained in the range of 0.998 to 1.027. Notably, C_D was close to 1.000 for b = 150 mm (P = 0.051) and b = 180 mm (P = 0.043). The St values in Table 7 show a similar pattern to C_D, reaching a nearly constant value at high b values or low P values. The results suggest that C_D and St are largely unaffected beyond certain b or P values, while ξ shows a consistent tendency to either increase or decrease. For comparison, Figure 5 and Table 7 show additional ξ values calculated using Equations (1), (2), and (3) proposed by Kirschmer [24], Meusburger [2], and Böttcher et al. [29], respectively. In Equations (1) and (2), k_F was defined as 1.79, as proposed by Kirschmer [24] for circular bar shapes. Furthermore, due to the perpendicular inflow conditions, α and β were both set to 90°, and δ was set to 0°. Since the study did not examine rack clogging, k_V was set to 1. The comparison showed minimal variation in ξ. Specifically, the ξ values calculated by LES for low b or high P were generally lower than those obtained by the empirical formulas. Conversely, the empirical formulas resulted in lower ξ values for high b or low P values. To quantify the differences, the root mean square relative errors (RMSREs) for ξ were calculated and were 18.5%, 39.1%, and 15.3% using Equation (13) compared to Equations (1), (2), and (3), respectively. In addition to Equation (13), ξ was also calculated based on C_D using Equation (14), with the results presented in Table 7. A high degree of agreement was obtained with an RMSRE of 1.3% using Equations (13) and (14), with the most notable deviations found at relatively high b or low P values.

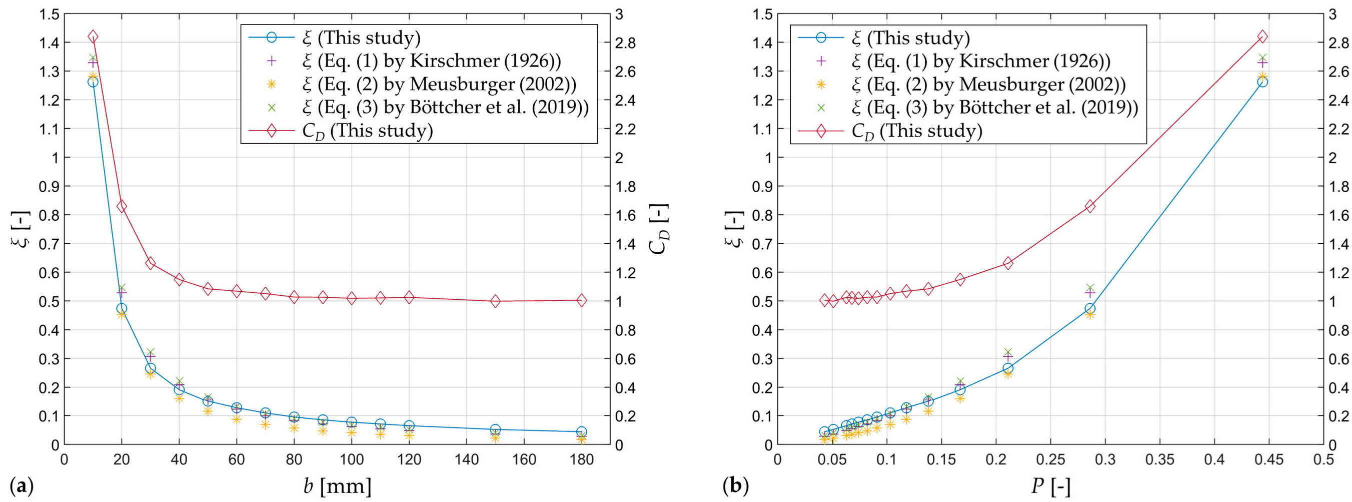

Figure 5. The drag coefficient C_D and the head loss coefficient ξ, calculated using Equation (13), as functions of (**a**) the clear bar spacing b and (**b**) the blocking ratio P, compared to ξ, calculated using Equations (1), (2), and (3) proposed by Kirschmer [24], Meusburger [2], and Böttcher et al. [29], respectively.

Table 7. Results of varying the clear bar spacing b or the blocking ratio P to determine the drag coefficient C_D, the Strouhal number St, and the head loss coefficient ξ, calculated using Equations (1), (2), and (3) proposed by Kirschmer [24], Meusburger [2], and Böttcher et al. [29], respectively, and Equations (13) and (14) based on the results of the numerical simulations.

b [mm]	P [-]			ξ [-]			C_D [-]	St [-]
		Equation (1)	Equation (2)	Equation (3)	Equation (13)	Equation (14)		
10	0.444	1.329	1.281	1.347	1.262	1.262	2.840	0.296
20	0.286	0.528	0.453	0.547	0.474	0.474	1.659	0.244
30	0.211	0.307	0.246	0.323	0.266	0.266	1.262	0.240
40	0.167	0.209	0.160	0.222	0.191	0.191	1.149	0.230
50	0.138	0.155	0.115	0.166	0.150	0.150	1.084	0.226
60	0.118	0.122	0.087	0.131	0.127	0.126	1.068	0.224
70	0.103	0.099	0.069	0.107	0.109	0.108	1.051	0.216
80	0.091	0.083	0.057	0.090	0.095	0.093	1.027	0.216
90	0.082	0.071	0.047	0.077	0.085	0.084	1.026	0.212
100	0.074	0.062	0.041	0.067	0.077	0.075	1.018	0.214
110	0.068	0.054	0.035	0.060	0.071	0.069	1.021	0.212
120	0.063	0.048	0.031	0.053	0.065	0.064	1.025	0.212
150	0.051	0.036	0.022	0.040	0.052	0.051	0.998	0.212
180	0.043	0.028	0.017	0.031	0.044	0.043	1.005	0.212

3.3. Effect of Flow Velocity

In the previous sections, U_1 was fixed at 0.5 m/s, resulting in Re_b = 3981. Here, U_1 was varied to examine its effect on the results. Figures 6a and 6b show the results for ξ and C_D, respectively. In addition, the results for the case of b = 90 mm are listed in Table 8, while the results for b = 10, 20, and 30 mm are given in Appendix A. The results show a velocity-dependent behavior within the velocity ranges tested. Reducing U_1 to 0.3 and 0.4 m/s for b = 10, 20, and 90 mm (P = 0.444, 0.286, and 0.082, respectively) led to a decrease in both ξ and C_D compared to U_1 = 0.5 m/s, which was not observed for b = 30 mm (P = 0.211). For all b values tested when $U_1 \geq 0.5$ m/s, ξ and C_D generally increased. For example, doubling U_1 from 0.5 to 1.0 m/s for b = 90 mm (P = 0.082) resulted in a 15.8% increase in ξ and a 15.7% increase in C_D. For comparison, Figure 6a also shows the ξ values calculated using Equation (1) proposed by Kirschmer [24], which does not take flow velocity into account, similar to Equation (2) by Meusburger [2] and (3) by Böttcher et al. [29]. Thus, ξ

remained constant as U_1 was varied. Consistent with Section 3.2, the use of Equation (14) to determine ξ showed excellent agreement with an RMSRE of 0.7% compared to Equation (13) for all b and U_1 values tested. In contrast to ξ and C_D, St mainly decreased or remained nearly constant with increasing U_1.

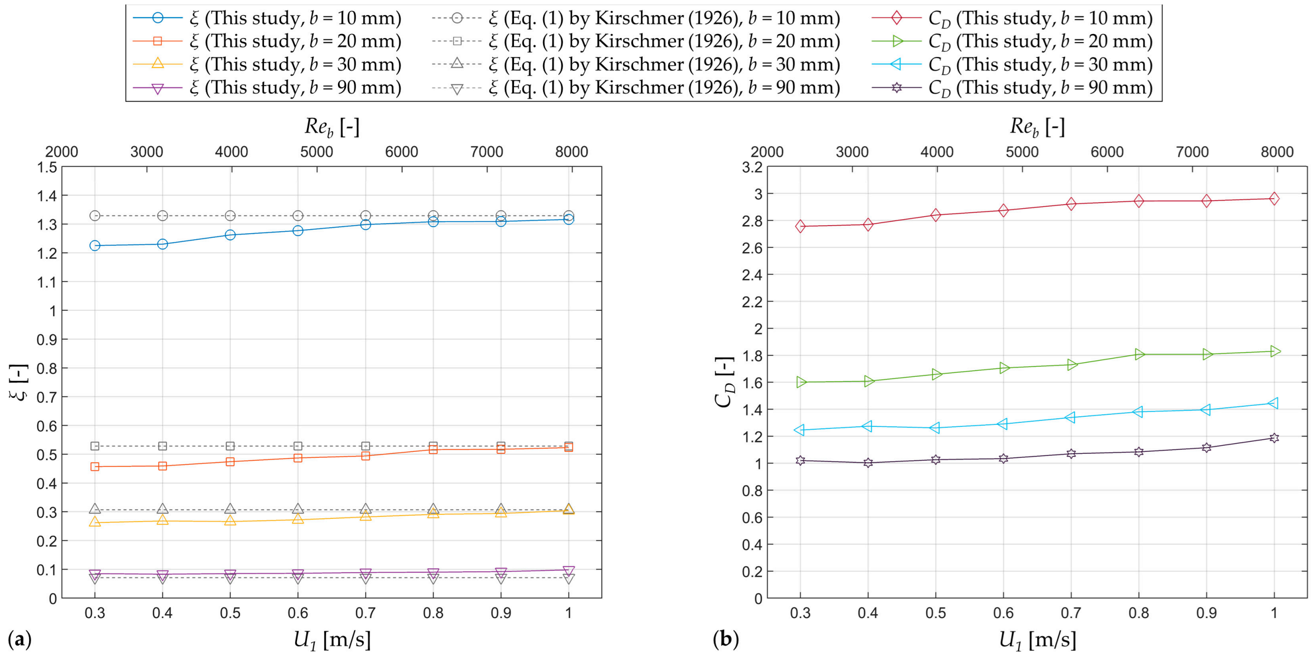

Figure 6. (**a**) The drag coefficient C_D and (**b**) the head loss coefficient ξ, calculated using Equation (13), as functions of the flow velocity at the inlet U_1 and the bar Reynolds number Re_b, compared to ξ calculated using Equation (1) proposed by Kirschmer [24].

Table 8. Results of varying the flow velocity at the inlet U_1 or the bar Reynolds number Re_b for the clear bar spacing b = 90 mm or the blocking ratio P = 0.082 to determine the drag coefficient C_D, the Strouhal number St, and the head loss coefficient ξ, calculated using Equation (1) proposed by Kirschmer [24] and Equations (13) and (14) based on the results of the numerical simulations.

U_1 [m/s]	Re_b [-]	b [mm]	P [-]	ξ (MRE) [-] Equation (1)	Equation (13)	Equation (14)	C_D (MRE) [-]	St [-]
0.3	2,389			0.071 (±0.0%)	0.085 (−0.5%)	0.083 (−0.6%)	1.020 (−0.6%)	0.216
0.4	3,185			0.071 (±0.0%)	0.083 (−2.1%)	0.082 (−2.2%)	1.003 (−2.2%)	0.216
0.5	3,981			0.071 (Ref.)	0.085 (Ref.)	0.084 (Ref.)	1.026 (Ref.)	0.212
0.6	4,777			0.071 (±0.0%)	0.086 (+0.8%)	0.084 (+0.8%)	1.034 (+0.8%)	0.212
0.7	5,573	90	0.082	0.071 (±0.0%)	0.089 (+4.4%)	0.087 (+4.3%)	1.070 (+4.3%)	0.210
0.8	6,369			0.071 (±0.0%)	0.090 (+5.8%)	0.089 (+5.7%)	1.084 (+5.7%)	0.211
0.9	7,166			0.071 (±0.0%)	0.092 (+8.6%)	0.091 (+8.6%)	1.115 (+8.6%)	0.208
1.0	7,962			0.071 (±0.0%)	0.098 (+15.8%)	0.097 (+15.7%)	1.187 (+15.7%)	0.208

4. Discussion

4.1. Interpretation of the Results in Relation to Previous Studies of Flow Past Circular Cylinders

The availability of a considerable amount of previous research on flow past circular cylinders with comparable Re_b was a major advantage of the present study. Thus, several settings and model parameters were adopted in this study, including the definition of $L_{x,us}$ as 10s (similar to, e.g., [85,91]), L_y as 4s (similar to, e.g., [75,100]), N_c as 240, N_r as 64 (both similar to, e.g., [64]), and N_y as 80 (similar resolution to, e.g., [89]). In contrast, a value of 100s was used for $L_{x,ds}$, which is significantly higher than in previous studies, because in this study, ξ was calculated based on p_1 and p_2 at the inlet and outlet, respectively, using

Equation (13), and to keep $\alpha_{kin,2}$ as close to unity as possible. In Section 3.1, independence tests confirmed the suitability of the selected reference case values. Furthermore, a simplified 2D scenario was investigated by defining $N_y = 1$. The results were comparable to those of Khan et al. [64], as the C_D value was overestimated. This is in accordance with the findings of Beaudan and Moin [66] that 3D effects occur at $Re_b = 3900$, such as pairs of counter-rotating streamwise vortices, which cannot be represented in 2D simulations. In addition, Lu et al. [100] observed both streamwise and spanwise vortices in the wake of the cylinder. It should also be noted that the ANSYS Fluent User's Guide [101] recommends the use of 3D numerical simulations for LES. As shown in Figure 4a and comparable to previous research (e.g., [72,100]), unsteady flow conditions in the wake of the cylinder resulted in time-dependent fluctuations of relevant flow parameters such as ξ_f and C_{Df}. Therefore, the calculation of time–mean (or time-averaged) values over an appropriate time period is crucial. Interestingly, increased turbulence in the same region has led to the measurement of fluctuating flow parameters downstream of CBTRs in model experiments, as reported by Böttcher et al. [29].

The use of multiple bars or periodic top and bottom boundary conditions produced divergent results compared to the single-bar reference case at low b or high P values, but this effect diminished with increasing b or decreasing P. According to Afgan et al. [85], two side-by-side cylinders at $Re_b = 3000$ and $P \leq 0.500$ behave independently, exhibiting symmetric wake patterns and antiphase vortex shedding. However, the interaction of the Kármán vortex streets in the wake of the cylinders can still affect C_D and St [83]. As P continues to decrease, the results of two side-by-side cylinders tend to approach those of a single cylinder, with no perturbation observed at P values less than 0.200 to 0.250 [84]. The results listed in Table 7 support this trend, although an MRE below the predefined threshold was only achieved for $b \geq 50$ mm or $P \leq 0.138$. Nevertheless, this is strongly related to the threshold definition and other factors such as the definition of $L_{x,ds}$. Significant differences were found when comparing the results of the DES model, the Smagorinsky–Lilly and dynamic Smagorinsky–Lilly LES models, and the URANS approach in Section 3.1.6, especially for $b = 90$ mm ($P = 0.082$). Thus, it can be concluded that the URANS approach is not suitable to accurately predict C_D, while the DES and LES models give comparable results, as stated in Section 1. However, for $b = 10$ mm ($P = 0.444$), the C_D and St values calculated using the URANS approach were close to those of the reference case, suggesting that this conclusion may not be valid for low b or high P values and highlighting the need for further research to address this issue.

As shown in Section 3.2, a decrease in b or an increase in P resulted in an increase in C_D and St values when $P \geq 0.103$, which is consistent with previous research on flow past confined cylinders [86–88]. Conversely, C_D remained relatively constant when $P \leq 0.091$, except for the cases when b was 150 and 180 mm ($P = 0.051$ and 0.043, respectively), where slightly lower C_D values were obtained. This may align with the recommendation of Nguyen et al. [86] that P should be limited to less than 0.05 for confined cylinders with no-slip walls to minimize wall effects on the results. In Section 3.3, a velocity-dependent behavior of C_D and St was shown. Specifically, at lower velocities between 0.3 and 0.5 m/s, C_D remained almost constant, but increased from 0.5 m/s (corresponding to $Re_b = 3981$) to 1.0 m/s (corresponding to $Re_b = 7962$) for all b values tested. Similar results have previously been found in this Re_b range for flow past a circular cylinder [102,103]. Typically, as Re_b continues to increase, C_D maintains a relatively constant value of about 1.2 [102] until it reaches the so-called drag crisis at $Re_b \approx 200{,}000$ to 300,000, where C_D drops abruptly [104–106]. In addition, increasing Re_b in this study generally led to a decrease in St, which has also been observed in previous studies [107]. This behavior can be attributed to the transition from laminar to turbulent flow, which shifts from the wake region to the point of flow separation at the cylinder surface with increasing Re_b [67].

4.2. Interpretation of the Results in Relation to Previous Studies for Determining Head Loss Coefficients of Trash Racks

Consistent with previous experimental studies (e.g., [2,24,29]), the results in Section 3.2 showed a progressive decrease in ξ with increasing b or decreasing P. The ξ values obtained from the numerical simulations were generally in good agreement with those obtained using the empirical formulas, with RMSREs ranging from 15.3% (with respect to Equation (3)) to 39.1% (with respect to Equation (2)). For comparison, Albayrak et al. [46] reported a mean prediction error of 16% when comparing their proposed prediction equation for ξ with the corresponding measurement results. The differences observed in this study can be attributed, on the one hand, to the P values between 0.134 and 0.535 [24], 0.190 and 0.550 [2], and 0.250 and 0.500 (without transversal elements) [29] tested in the studies from which the Equations (1), (2), and (3), respectively, were derived. Accordingly, these empirical formulas were not intended for low P values, such as those between 0.043 and 0.118 (b between 60 and 180 mm) examined in this study. Based on the good agreement of the C_D and St results with previous research on flow past a cylinder, as discussed in Section 4.1, this may imply that the numerically obtained ξ values are more accurate for relatively low P ranges. Nevertheless, further research is needed to confirm this. On the other hand, in the experiments with CBTRs by Böttcher et al. [29], flow-induced vibrations of the bars were observed, especially at high P values. Although additional spacers were used, it could not be excluded that ξ was affected [29]. Typically, circular bars are highly susceptible to flow-induced vibrations [108]. However, the rigid and stationary bars used in this study did not allow for any effects of flow-induced vibrations on ξ. This may explain why the numerically obtained ξ values at low b or high P values are lower than those obtained using the empirical formulas. Overall, the relative differences in ξ were higher for high b or low P values.

The use of three or five bars in Section 3.1.5 resulted in a decrease in ξ compared to the use of a single bar in the computational domain. While the results appear to be significantly different, with MREs up to 6.0% for ξ, the deviations are in a comparable range to those obtained numerically and using the empirical formulas. For example, for b = 10 mm (P = 0.444) and n = 1, a deviation of 6.7% was observed compared to the values obtained using Equation (3). Thus, the use of n = 1 seems to be appropriate for an initial estimation of ξ. However, larger differences were observed when periodic top and bottom boundary conditions were applied, especially for b = 10 mm, which resulted in an MRE of 15.9% for ξ. Increasing n led to further reductions in ξ, but only for relatively low b or high P values. The results in Section 3.1.5 indicate a correlation between n and ξ that appears to decrease as b increases or P decreases, which is in line with the behavior of n and C_D discussed in Section 4.1. Implementing periodic boundary conditions can generally reduce the influence of the walls on the wake behind the cylinders, but it may not fully account for potential interactions between individual bars compared to using multiple bars. A similar approach was used by Åkerstedt et al. [49], where a single-bar domain with periodic boundary conditions in the symmetry plane between the bars was able to produce comparable ξ values to domains consisting of more than 20 bars. Whether this finding holds true for the approach presented in this study requires further investigation.

Many commonly used empirical formulas for determining ξ do not account for the effect of U_1 or Re_b on the results [33], including Equation (3) by Böttcher et al. [29]. Through experimental studies with CBTRs, Böttcher et al. [29] found that ξ is largely unaffected by U_1 when $Re_b \geq 750$. However, their investigation only covered Re_b values between 750 and 3000. In this study, the Re_b values tested ranged from 2389 to 7962. No clear trend for ξ was found for $Re_b \leq 3185$ (corresponding to $U_1 \leq 0.4$ m/s), which is in agreement with the results of Böttcher et al. [29]. Conversely, a velocity-dependent behavior was observed for $Re_b \geq 3981$ (corresponding to $U_1 \geq 0.5$ m/s), as described in Section 3.3. Specifically, as U_1 increased from 0.5 to 1.0 m/s (corresponding to Re_b from 3981 to 7962), ξ increased by 15.8% for b = 90 mm (P = 0.444). As discussed in Section 4.1, these increases are consistent with the velocity-dependent behavior of C_D in previous studies of flow past a circular cylinder. It is important to note that this behavior is not universally applicable to non-circular bar shapes. Bar shapes with sharp edges, such as rectangular, square, or triangular shapes, typically experience flow separation at the fixed sharp edges due to the abrupt change in geometry, making the flow characteristics relatively insensitive to Re_b [107,109,110]. Circular shapes, on the other hand, exhibit a back-and-forth oscillation of the flow separation point on the cylinder surface [109] and have therefore received more attention in the past [63,107]. In terms of head losses, rectangular bar shapes generally give higher ξ values, while rounded edges give considerably lower ξ values [15,24,32,45]. Taking into account previous findings on flow past non-circular cylinders (e.g., [110–112]), future research should include numerical simulations using non-circular bar shapes. This may lead to the development of customized formulas for different bar shapes, similar to Meister et al. [32], who provided two ξ prediction formulas, one for rectangular bar shapes and another for streamlined bar shapes.

The numerical simulations in this study focused on submerged bars, thus ignoring the effect of the free surface on the results. In contrast, most previous experimental studies used open-channel flow conditions (e.g., [24,29]). Meusburger [2] analyzed ξ in both open-channel flow and closed-pipe flow under laboratory conditions and found that the ξ values for both types of flow are comparable, with insignificant deviations within the range of measurement accuracy. In addition, Clark et al. [45] performed experiments in pressurized rectangular conduits and compared the results with ξ values of established empirical formulas developed based on open-channel flow conditions. Their results indicate that the formulas are also applicable to submerged trash racks. Therefore, it can be assumed that the results of this study are also valid for CBTRs in open-channel flow conditions. However, since neither Meusburger [2] nor Clark et al. [45] studied the circular bar shape, future research should investigate CBTRs in open-channel flow conditions, taking into account existing studies on flow past a circular cylinder near a free surface (e.g., [113]).

Although this study was only superficially concerned with flow behavior, the results showed pressure curves in the streamwise direction analogous to those of Clark et al. [45], indicating a constant pressure level upstream and mostly uniform flow conditions far downstream of the rack section. For a more comprehensive understanding of the flow behavior near CBTRs, the extensive literature on flow past cylinders can be a helpful reference, where the flow behavior has been studied in detail (e.g., [67,69,100]).

4.3. Further Limitations and Potential Future Research Topics

Cost-effective numerical analysis of complex problems requires the setting of assumptions and constraints. At the same time, simulations and their results can be significantly affected by various factors such as input data, model parameters, SGS, computational domain, and grid resolution [114]. For instance, the findings of this study suggest that the use of a more sophisticated model than the URANS approach in 3D numerical simulations would be beneficial to the problem at hand. In this context, it is important to note that the numerical simulations for the method comparison in Section 3.1.6 used the same model settings as the reference model in terms of domain, grid, and time issues, without performing additional independence studies. Consequently, there were also no significant differences in computational time between the simulations. Overall, all simulations required a considerable amount of time to complete. The reference case specified in Section 3.1 with b = 10 mm (P = 0.444) took about twelve days, while the simulation with the longest computation time, which also included the largest N_t (i.e., the case described in Section 3.1.5 with b = 30 mm or P = 0.211 and n = 5), took about 100 days. The computational cost generally increased with increasing b or decreasing P, as well as with increasing U_1. Regarding the variations in U_1 described in Section 3.3, it is noteworthy that U_1 has a direct correlation with several numerical parameters, including y^+, which increased almost linearly with U_1. As a result, y^+ values of one or even higher were observed for a small number of elements in the computational domains, specifically for b = 10 mm (P = 0.444) at $U_1 \geq 0.7$ m/s, b = 20 mm (P = 0.286) at $U_1 \geq 0.9$ m/s, and b = 30 and 90 mm (P = 0.211 and

0.082, respectively) at U_1 = 1.0 m/s. However, since the number of elements with $y^+ \geq 1$ was very small, it can be assumed that the effect on the results is negligible. In addition to U_1, the friction coefficients also affect the y^+ values. Therefore, the friction coefficients for the bars surfaces were kept constant in all simulations by using the default friction value in ANSYS Fluent 19.2 [101].

Previous experimental studies have analyzed the effect of spacers and other support structures on ξ (e.g., [2,115]), which were not considered in the present study. Similarly, this study did not examine the effects of clogging (e.g., [2,9]) or bottom and top overlays (e.g., [15,32]), nor did it consider bars with non-perpendicular inflow conditions. Such bars are important for fish guidance racks, which typically consist of bars angled to either the side wall or the ground plane to guide downstream migrating fish to an appropriate bypass [9,10,13,14,18]. Furthermore, many empirical equations are based on undisturbed, uniform inflow conditions [116]. However, inflow conditions to trash racks at HPPs are much more complex [117,118] and also depend on the design of the HPP [2,32]. This highlights the importance of future studies investigating cylinders angled with respect to the approach flow direction. Previous research, especially on flow past inclined or yawed cylinders (e.g., [119–121]), can serve as a basis. Beyond that, the implementation of rack configurations that deflect the flow, including angled bar racks, louvers [25,46,122], and curved bar racks (CBRs) [30,123], may present challenges in the current approach and will require additional research in the future.

Few experimental studies have investigated scale effects in the context of trash racks, resulting in only anecdotal findings (e.g., [15,46]). In general, achieving satisfactory similarity between physical scale models and their real-world counterparts can be challenging [124]. Therefore, scale effects represent another potential area for further research. This includes the effect of s on the results, which in this study was defined as a constant of 8 mm to reduce computational cost and achieve a Re_b value close to 3900. According to Kirschmer [24], the effect of s on the results is negligible for bars under frontal inflow conditions if the ratio of s to b remains constant. Thus, the use of 8 mm seems appropriate for this study, but its applicability should be re-evaluated in possible future studies.

4.4. Transferability to Applications in Research and Engineering Practice

Besides the limitations described in the previous sections, the presented approach also offers advantages over experimental studies. In physical model tests under open-channel flow conditions, trash racks result in small head losses relative to water depth, in some cases, comparable to the measurement accuracy of the instruments used. Water level fluctuations during high discharges further complicate measurements [29]. Thus, the determination of head losses can be difficult. Conversely, under pressurized pipe flow conditions, piezometers are generally used to measure the pressure differences upstream and downstream of the rack, as performed by Clark et al. [45], thereby determining head losses or ξ in a manner comparable to this study. This also allows the neglect of U_2 in the calculation of ξ, which can have a significant effect on the results in open-channel experiments [33]. However, for the determination of ξ in experimental studies, it is critical to account for continuous losses due to friction and local losses due to spacers or support structures. Lučin et al. [31] stated that experimental studies using open-channel flow conditions tend to overestimate ξ due to shallow water depths compared to the actual geometries at HPPs, resulting in a more pronounced influence of bottom flow resistance on ξ. Furthermore, especially in scenarios with considerable lateral flow deflections, the effect of restricted width in physical model tests on ξ is worth investigating. The critical question is whether the use of periodic boundary conditions in numerical simulations provides a more accurate representation of reality than the restricted width in experimental studies.

The combination of physical model tests and numerical simulations can offer notable advantages, including increased availability of hydraulic parameter data and reduced cost and time, compared to relying solely on physical model tests. For instance, Leuch et al. [50] validated their numerical simulations using results from previous experimental model tests [30,122] and numerically investigated a more streamlined bar shape for a CBR. Similarly, future research can determine ξ values for new or modified bar shapes, such as bars with electrodes attached to the side or front for upgrading existing racks to hybrid barriers [125]. In terms of numerical analysis, this study showed that the implementation of trash racks in 3D numerical models of HPPs is only feasible in a simplified manner due to the requirement of very fine grid discretization and hence significant computational effort when using the LES model. Alternatively, practical solutions involve the use of baffles or porous media with ξ values as input data [118,126–128]. In general, the most appropriate approach depends on the level of detail required for the specific problem.

While authorities in some countries require low b values for physical barriers to improve fish protection, such as several German federal states with $b \leq 20$ mm [129], higher b values may become decisive when hybrid or mechanical barriers are used. However, commonly used empirical formulas for the calculation of ξ are mainly based on a limited number of investigated parameters, as discussed in Section 4.2 for b or P. Consequently, the formulas are not universally applicable to all rack configurations. The findings of this study provide a better understanding of ξ for relatively high b values. Nevertheless, further research is needed to propose new prediction formulas for ξ or to adjust existing empirical formulas to account for high b values. Equation (14) provides a simplified approach for determining ξ in cases with high b or low P values, as indicated by the low RMSREs for ξ using Equations (13) and (14) in this study. Considering that C_D remains relatively constant in certain P ranges, such as $P \leq 0.091$ for circular bar shapes at U_1 = 0.5 m/s, as described in Section 3.2, ξ can be estimated by referring to established C_D values from the existing literature and using the P value of the corresponding trash rack.

Finally, this study focused on trash racks located upstream of HPPs. However, racks or similar structures are used in various engineering settings, such as wastewater treatment plants and pumping stations [33]. The results of this study may be also applicable to other types of racks. In addition, the results of the independence tests presented in Section 3.1 provide a valuable resource for future studies of flow past (confined) cylinders, particularly when free-slip wall conditions are applied at the top and bottom of the computational domain.

5. Conclusions

The present study used 3D numerical simulations to analyze the head loss coefficients ξ of circular bar trash racks (CBTRs), mainly including a single bar with a bar thickness s of 8 mm in the computational domain and applying the Large Eddy Simulation (LES) model. In detail, bars oriented perpendicular to the flow direction were studied under homogeneous inflow conditions. Furthermore, the effects of the clear bar spacing b and the flow velocity at the inlet of the computational domain U_1 on the results were investigated. The model settings for the simulations were established through an extensive analysis of the available literature on flow past circular cylinders, specifically at a Reynolds bar number Re_b of 3900, in addition to preliminary studies. These settings were then validated by systematic independence tests. Based on the results and their interpretation in relation to previous studies of flow past cylinders and experimental studies to determine ξ of trash racks, the following key findings were obtained:

- Well-resolved simulations using the LES model were able to calculate ξ of CBTRs with a degree of accuracy similar to that of the empirical formulas used for comparison. The Detached Eddy Simulation (DES) model, although used only briefly in this study, showed similar potential. In contrast, the unsteady Reynolds-averaged Navier–Stokes (URANS) approach produced divergent results, especially when compared to previous research on flow past unconfined cylinders. Furthermore, the flow parameters analyzed indicate that the problem is primarily 3D in nature. Therefore, future research in this area should be based on 3D numerical simulations rather than 2D models.
- For relatively low blocking ratios P, the presented approach accurately calculated ξ of CBTRs, as confirmed by comparison with previous studies on flow past circular

cylinders. Conversely, the empirical formulas of Kirschmer [24], Meusburger [2], and Böttcher et al. [29] tended to underestimate ξ in such cases. The fact that these formulas were not intended to be used when $P < 0.134$ may account for these differences. In addition, Equation (14) can be used for a simple calculation of ξ when the drag coefficient C_D is known, for example, from previous studies of flow past cylinders, especially for low P values. In this study, C_D remained relatively constant for $U_1 = 0.5$ m/s when $P \leq 0.091$ ($b \geq 80$ mm).

- For relatively high P values, especially for $P = 0.444$ ($b = 10$ mm), ξ was underestimated compared to the empirical formulas used for comparison. The differences can be attributed to the neglect of important effects in the numerical simulations, such as flow-induced vibrations. Furthermore, comparisons with simulations using three and five bars in the domain or periodic boundary conditions at the top and bottom of the domain showed that an acceptable level of independence for high P values could not be achieved with the presented approach.
- While ξ remained relatively constant for U_1 between 0.3 and 0.5 m/s, it increased continuously for $U_1 \geq 0.5$ m/s (corresponding to $Re_b \geq 3981$) and all b values tested. This finding is consistent with previous research on flow past circular cylinders in terms of C_D, but cannot be directly applied to non-circular bar shapes due to the different flow patterns that occur depending on the cross-sectional shape [63,107].

In addition to the limitations of the study, the potential of the presented approach for future research was discussed in detail in Section 4, which may include detailed studies of angled bars or novel bar shapes. Advancements in this approach may help to determine ξ in various applications, thereby enhancing the overall understanding of head losses at trash racks.

Funding: This research received no external funding.

Data Availability Statement: The data presented in this study are available on request from the author. The data are not publicly available due to ongoing research.

Acknowledgments: The computational results presented here have been achieved using the LEO HPC infrastructure of the University of Innsbruck.

Conflicts of Interest: The author declares no conflicts of interest.

Abbreviations

CBR	Curved bar rack
CBTR	Circular bar trash rack
CFD	Computational Fluid Dynamics
DES	Detached Eddy Simulation
DNS	Direct Numerical Simulation
FFT	Fast Fourier Transform
HPC	High-performance computing
HPP	Hydropower plant
LES	Large Eddy Simulation
MRE	Mean relative error
RANS	Reynolds-averaged Navier–Stokes
RMSRE	Root mean square relative error
SGS	Subgrid-scale
SIMPLE	Semi-Implicit Method for Pressure-Linked Equations
SST	Shear Stress Transport
URANS	Unsteady Reynolds-averaged Navier–Stokes

Notations

A	Area [m^2]
b	Clear bar spacing [m]
C_D	Drag coefficient [-]
C_L	Lift coefficient [-]
C_s	Smagorinsky coefficient [-]
F_D	Drag force on the cylinder [N]
F_L	Lift force on the cylinder [N]
f_v	Vortex shedding frequency [1/s]
g	Gravitational acceleration [m/s^2]
h_v	Local head loss [m]
k_F	Bar shape coefficient by Kirschmer [24] [-]
k_r	Resolved turbulent kinetic energy [m^2/s^2]
k_t	Total turbulent kinetic energy [m^2/s^2]
k_V	Loss factor to account for sectional clogging of the rack [-]
LES_{IQ}	LES index of quality [-]
$LES_{IQ,avg}$	Volume-averaged mean value of LES index of quality [-]
$LES_{IQ,min}$	Minimum value of LES index of quality for all evaluated time steps [-]
L_x	Length of the domain in the streamwise direction [m]
$L_{x,ds}$	Length of the domain downstream of the rack section in the streamwise direction [m]
$L_{x,us}$	Length of the domain upstream of the rack section in the streamwise direction [m]
L_y	Length of the domain in the spanwise direction [m]
L_z	Length of the domain in the vertical direction [m]
n	Number of bars in the computational domain [-]
N_c	Number of elements on the bar circumference [-]
N_r	Number of elements in the radial direction of the near-field grid [-]
N_t	Total number of elements in the computational domain [-]
N_y	Number of elements in the spanwise direction [-]
P	Blocking ratio [-]
p	Pressure [N/m^2]
p_1, p_2	Pressure at the inlet and outlet of the computational domain, respectively [N/m^2]
q	Unit discharge [m^2/s]
Re_b	Bar Reynolds number [-]
$\lvert S \rvert$	Characteristic filtered rate of strain [1/s]
s	Bar thickness [m]
S_{ij}	Resolved rate of the strain tensor [1/s]
St	Strouhal number [-]
T	Vortex shedding cycle [s]
t	Time [s]
t_e	Evaluation time [s]
U	Flow velocity [m/s]
U_{ref}	Free-stream velocity or the undisturbed flow velocity upstream of the rack [m/s]
U_1, U_2	Flow velocity at the inlet and outlet of the computational domain, respectively [m/s]
u, v, w	Flow velocity components in x-, y- and z-direction, respectively [m/s]
x, y, z	Cartesian coordinates [-]
y^+	Dimensionless distance from the wall [-]
z_1, z_2	Elevation at the inlet and outlet of the computational domain, respectively [m]
α	Rack angle relative to the side wall [°]
α_{kin}	Kinetic energy correction factor [-]
$\alpha_{kin,1}, \alpha_{kin,2}$	Kinetic energy correction factor at the inlet and outlet of the computational domain, respectively [-]
β	Rack angle relative to the ground plane [°]
Δ	Grid size defining the subgrid length scale [m]
Δt	Time step [s]
δ	Horizontal inflow angle to the rack [°]
δ_{ij}	Kronecker delta symbol [-]

ν	Kinematic viscosity [m^2/s]
ν_{sgs}	Subgrid-scale eddy viscosity [m^2/s]
ξ	Head loss coefficient [-]
ξ_n	Time-averaged normalized head loss coefficient [-]
ρ	Fluid density [kg/m^3]
τ_{ij}	Subgrid-scale (SGS) stress tensor [N/m^2]

Appendix A

Table A1. Results of varying the flow velocity at the inlet U_1 or the bar Reynolds number Re_b for the clear bar spacings b = 10, 20, and 30 mm or the blocking ratios P = 0.444, 0.286, and 0.211 to determine the drag coefficient C_D, the Strouhal number St, and the head loss coefficient ξ, calculated using Equation (1) proposed by Kirschmer [24] and Equations (13) and (14) based on the results of the numerical simulations.

U_1 [m/s]	Re_b [-]	b [mm]	P [-]	ξ (MRE) [-] Equation (1)	Equation (13)	Equation (14)	C_D (MRE) [-]	St [-]
0.3	2389	10	0.444	1.329 (±0.0%)	1.225 (−2.9%)	1.225 (−3.0%)	2.756 (−3.0%)	0.306
0.4	3185			1.329 (±0.0%)	1.230 (−2.5%)	1.231 (−2.5%)	2.769 (−2.5%)	0.302
0.5	3981			1.329 (Ref.)	1.262 (Ref.)	1.262 (Ref.)	2.840 (Ref.)	0.296
0.6	4777			1.329 (±0.0%)	1.277 (+1.2%)	1.277 (+1.2%)	2.874 (+1.2%)	0.290
0.7	5573			1.329 (±0.0%)	1.298 (+2.9%)	1.299 (+2.9%)	2.922 (+2.9%)	0.291
0.8	6369			1.329 (±0.0%)	1.308 (+3.7%)	1.308 (+3.7%)	2.944 (+3.7%)	0.291
0.9	7166			1.329 (±0.0%)	1.309 (+3.7%)	1.309 (+3.7%)	2.945 (+3.7%)	0.292
1.0	7962			1.329 (±0.0%)	1.316 (+4.3%)	1.316 (+4.3%)	2.962 (+4.3%)	0.291
0.3	2389	20	0.286	0.528 (±0.0%)	0.457 (−3.5%)	0.457 (−3.5%)	1.601 (−3.5%)	0.258
0.4	3185			0.528 (±0.0%)	0.459 (−3.0%)	0.460 (−3.1%)	1.608 (−3.1%)	0.254
0.5	3981			0.528 (Ref.)	0.474 (Ref.)	0.474 (Ref.)	1.659 (Ref.)	0.244
0.6	4777			0.528 (±0.0%)	0.487 (+2.8%)	0.487 (+2.8%)	1.706 (+2.8%)	0.246
0.7	5573			0.528 (±0.0%)	0.494 (+4.3%)	0.494 (+4.3%)	1.730 (+4.3%)	0.242
0.8	6369			0.528 (±0.0%)	0.516 (+9.0%)	0.516 (+9.0%)	1.808 (+9.0%)	0.235
0.9	7166			0.528 (±0.0%)	0.517 (+9.0%)	0.517 (+9.0%)	1.808 (+9.0%)	0.240
1.0	7962			0.528 (±0.0%)	0.523 (+10.3%)	0.523 (+10.3%)	1.830 (+10.3%)	0.236
0.3	2389	30	0.211	0.307 (±0.0%)	0.262 (−1.2%)	0.262 (−1.2%)	1.246 (−1.2%)	0.244
0.4	3185			0.307 (±0.0%)	0.268 (+1.0%)	0.268 (+1.0%)	1.274 (+1.0%)	0.240
0.5	3981			0.307 (Ref.)	0.266 (Ref.)	0.266 (Ref.)	1.262 (Ref.)	0.240
0.6	4777			0.307 (±0.0%)	0.272 (+2.3%)	0.272 (+2.3%)	1.291 (+2.3%)	0.232
0.7	5573			0.307 (±0.0%)	0.282 (+6.1%)	0.282 (+6.1%)	1.339 (+6.1%)	0.236
0.8	6369			0.307 (±0.0%)	0.291 (+9.4%)	0.291 (+9.4%)	1.381 (+9.4%)	0.233
0.9	7166			0.307 (±0.0%)	0.294 (+10.6%)	0.294 (+10.6%)	1.396 (+10.6%)	0.229
1.0	7962			0.307 (±0.0%)	0.304 (+14.5%)	0.304 (+14.5%)	1.445 (+14.5%)	0.229

References

1. Wahl, T.L. *Trash Control Structures and Equipment: A Literature Review and Survey of Bureau of Reclamation Experience*; U.S. Bureau of Reclamation: Denver, CO, USA, 1992.
2. Meusburger, H. *Energieverluste an Einlaufrechen von Flusskraftwerken*; ETH Zurich: Zurich, Switzerland, 2002. (In German) [CrossRef]
3. Giesecke, J.; Heimerl, S. *Wasserkraftanlagen: Planung, Bau und Betrieb*, 6th aktualisierte u. erw ed.; Springer: Berlin/Heidelberg, Germany, 2014; ISBN 978-3-642-53871-1. (In German)
4. Perham, R.E. *Floating Debris Control; A Literature Review*; US Army Cold Regions Research and Engineering Laboratory: Hanover, NH, USA, 1987.
5. Bradley, J.B.; Richards, D.L.; Bahner, C.D. *Debris Control Structures—Evaluation and Countermeasures*, 3rd ed.; Hydraulic Engineering Circular No. 9; U.S. Department of Transportation, Federal Highway Administration: Washington, DC, USA, 2005.
6. Schalko, I.; Schmocker, L.; Weitbrecht, V.; Boes, R.M. Backwater Rise Due to Large Wood Accumulations. *J. Hydraul. Eng.* **2018**, *144*, 04018056. [CrossRef]
7. Walczak, N. Operational Evaluation of a Small Hydropower Plant in the Context of Sustainable Development. *Water* **2018**, *10*, 1114. [CrossRef]
8. Hribernik, A. Evaluation of Clogged Hydropower Plant Trash Rack Losses. *SV-JME* **2020**, *66*, 142–152. [CrossRef]
9. Meister, J. *Fish Protection and Guidance at Water Intakes with Horizontal Bar Rack Bypass Systems*; ETH Zurich: Zurich, Switzerland, 2020. [CrossRef]

10. David, L.; Chatellier, L.; Courret, D.; Albayrak, I.; Boes, R.M. Fish Guidance Structures with Narrow Bar Spacing: Physical Barriers. In *Novel Developments for Sustainable Hydropower*; Rutschmann, P., Kampa, E., Wolter, C., Albayrak, I., David, L., Stoltz, U., Schletterer, M., Eds.; Springer International Publishing: Cham, Switzerland, 2022; pp. 91–98, ISBN 978-3-030-99137-1.
11. Čada, G.F.; Coutant, C.C.; Whitney, R.R. *Development of Biological Criteria for the Design of Advanced Hydropower Turbines*; U.S. Department of Energy, Idaho Operations Office: Idaho Falls, ID, USA, 1997.
12. Tsikata, J.M.; Tachie, M.F.; Katopodis, C. Open-Channel Turbulent Flow through Bar Racks. *J. Hydraul. Res.* **2014**, *52*, 630–643. [CrossRef]
13. Nielsen, N.; Szabo-Meszaros, M. *Hydropower and Fish—A Roadmap for Best Practice Management*; IEA: Paris, France, 2022. [CrossRef]
14. Ebel, G. *Fischschutz und Fischabstieg an Wasserkraftanlagen: Handbuch Rechen- und Bypasssysteme: Ingenieurbiologische Grundlagen, Modellierung und Prognose, Bemessung und Gestaltung; Mitteilungen aus dem Büro für Gewässerökologie und Fischereibiologie Dr. Ebel*, 3rd ed.; Büro für Gewässerökologie und Fischereibiologie Dr. Ebel: Halle, Germany, 2018; ISBN 978-3-00-039686-1. (In German)
15. Albayrak, I.; Maager, F.; Boes, R.M. An Experimental Investigation on Fish Guidance Structures with Horizontal Bars. *J. Hydraul. Res.* **2020**, *58*, 516–530. [CrossRef]
16. Larinier, M.; Travade, F. Downstream Migration: Problems and Facilities. *Bull. Fr. Pêche Piscic.* **2002**, 181–207. [CrossRef]
17. Williams, J.G.; Armstrong, G.; Katopodis, C.; Larinier, M.; Travade, F. Thinking like a Fish: A Key Ingredient for Development of Effective Fish Passage Facilities at River Obstructions: Fish Behaviour Related Fish Passage at Dams. *River Res. Applic.* **2012**, *28*, 407–417. [CrossRef]
18. Schwevers, U.; Adam, B. *Fish Protection Technologies and Fish Ways for Downstream Migration*; Springer International Publishing: Cham, Switzerland, 2020; ISBN 978-3-030-19241-9.
19. Meister, J.; Moldenhauer-Roth, A.; Beck, C.; Selz, O.M.; Peter, A.; Albayrak, I.; Boes, R.M. Protection and Guidance of Downstream Moving Fish with Electrified Horizontal Bar Rack Bypass Systems. *Water* **2021**, *13*, 2786. [CrossRef]
20. Tutzer, R.; Röck, S.; Walde, J.; Zeiringer, B.; Unfer, G.; Führer, S.; Brinkmeier, B.; Haug, J.; Aufleger, M. Ethohydraulic Experiments on the Fish Protection Potential of the Hybrid System FishProtector at Hydropower Plants. *Ecol. Eng.* **2021**, *171*, 106370. [CrossRef]
21. Haug, J.; Auer, S.; Frees, C.; Brinkmeier, B.; Tutzer, R.; Hayes, D.S.; Aufleger, M. Retrofitting of Existing Bar Racks with Electrodes for Fish Protection—An Experimental Study Assessing the Effectiveness for a Pilot Site. *Water* **2022**, *14*, 850. [CrossRef]
22. Haug, J.; Frees, C.; Brinkmeier, B.; Aufleger, M. Ethohydraulic Experiments Investigating Retention Rates of an Electrified Bar Rack. *Water* **2022**, *14*, 4036. [CrossRef]
23. Tutzer, R.; Röck, S.; Walde, J.; Haug, J.; Brinkmeier, B.; Aufleger, M.; Unfer, G.; Führer, S.; Zeiringer, B. A Physical and Behavioral Barrier for Enhancing Fish Downstream Migration at Hydropower Dams: The Flexible FishProtector. *Water* **2022**, *14*, 378. [CrossRef]
24. Kirschmer, O. *Untersuchungen über den Gefällsverlust an Rechen*; Mitteilungen des Hydraulischen Instituts der Technischen Hochschule München, Heft 1; Technische Hochschule München: Munich, Germany, 1926. (In German)
25. Raynal, S.; Courret, D.; Chatellier, L.; Larinier, M.; David, L. An Experimental Study on Fish-Friendly Trashracks—Part 1. Inclined Trashracks. *J. Hydraul. Res.* **2013**, *51*, 56–66. [CrossRef]
26. Raynal, S.; Chatellier, L.; Courret, D.; Larinier, M.; David, L. An Experimental Study on Fish-Friendly Trashracks—Part 2. Angled Trashracks. *J. Hydraul. Res.* **2013**, *51*, 67–75. [CrossRef]
27. Josiah, N.R.; Tissera, H.P.S.; Pathirana, K.P.P. An Experimental Investigation of Head Loss through Trash Racks in Conveyance Systems. *Engineer* **2016**, *49*, 1. [CrossRef]
28. Zayed, M.; El Molla, A.; Sallah, M. An Experimental Study on Angled Trash Screen in Open Channels. *Alex. Eng. J.* **2018**, *57*, 3067–3074. [CrossRef]
29. Böttcher, H.; Gabl, R.; Aufleger, M. Experimental Hydraulic Investigation of Angled Fish Protection Systems—Comparison of Circular Bars and Cables. *Water* **2019**, *11*, 1056. [CrossRef]
30. Beck, C.; Albayrak, I.; Meister, J.; Boes, R.M. Hydraulic Performance of Fish Guidance Structures with Curved Bars—Part 1: Head Loss Assessment. *J. Hydraul. Res.* **2020**, *58*, 807–818. [CrossRef]
31. Lučin, I.; Čarija, Z.; Grbčić, L.; Kranjčević, L. Assessment of Head Loss Coefficients for Water Turbine Intake Trash-Racks by Numerical Modeling. *J. Adv. Res.* **2020**, *21*, 109–119. [CrossRef]
32. Meister, J.; Fuchs, H.; Beck, C.; Albayrak, I.; Boes, R.M. Head Losses of Horizontal Bar Racks as Fish Guidance Structures. *Water* **2020**, *12*, 475. [CrossRef]
33. Baselt, I.; Malcherek, A. Determining the Flow Resistance of Racks and the Resulting Flow Dynamics in the Channel by Using the Saint-Venant Equations. *Water* **2022**, *14*, 2469. [CrossRef]
34. Latif, M.A.; Sarwar, M.K.; Farooq, R.; Shaukat, N.; Ali, S.; Hashmi, A.; Tariq, M.A.U.R. Estimating Energy Efficient Design Parameters for Trash Racks at Low Head Hydropower Stations. *Water* **2022**, *14*, 2609. [CrossRef]
35. Walczak, N.; Walczak, Z.; Tymiński, T. Laboratory Research on Hydraulic Losses on SHP Inlet Channel Trash Racks. *Energies* **2022**, *15*, 7602. [CrossRef]
36. Zayed, M.; El Molla, A.; Sallah, M. An Experimental Investigation of Head Loss through a Triangular "V- Shaped" Screen. *J. Adv. Res.* **2018**, *10*, 69–76. [CrossRef] [PubMed]
37. Spangler, J. *Untersuchungen Über den Verlust an Rechen Bei Schräger Zuströmung*; Mitteilungen des Hydraulischen Instituts der Technischen Hochschule München, Heft 2; Technische Hochschule München: Munich, Germany, 1928. (In German)
38. Berezinski, I. *Hydraulisches Handbuch*; Mostov, M.A.: Moscow, Russia, 1954. (In German)

39. United States Army Corps of Engineers (USACE). *Hydraulic Design Criteria*; USACE Waterways Experiment Station: Vicksburg, MS, USA, 1988.
40. Fellenius, W.; Lindquist, E.G.W. Experiments on the Head Loss Caused by Protecting Racks at Water-Power Plants. In *Hydraulic Laboratory Practice*; American Society of Mechanical Engineers (ASME): New York, NY, USA, 1929; pp. 533–538.
41. Escande, L. *Pertes de Charge a La Traversèe des Grilles*; Complements d'Hydraulique 1, Publications de l'Institut Electronique et de l'Institut de Mécanique des Fluides de l'Universté de Toulouse: Toulouse, France, 1947. (In French)
42. Orsborn, J.F. Rectangular-Bar Trashrack and Baffle Headlosses. *J. Power Div.* **1968**, *94*, 111–123. [CrossRef]
43. Zimmermann, J. *Widerstand Schräg Angeströmter Rechengitter*; Universität Fridericana Karlsruhe, Theodor-Rhebock-Flußbaulaboratorium, Mitteilungen Heft 157: Karlsruhe, Germany, 1969. (In German)
44. Bureau of Reclamation. *Design of Small Dams*, 3rd ed.; U.S. Department of the Interior: Denver, CO, USA, 1987.
45. Clark, S.P.; Tsikata, J.M.; Haresign, M. Experimental Study of Energy Loss through Submerged Trashracks. *J. Hydraul. Res.* **2010**, *48*, 113–118. [CrossRef]
46. Albayrak, I.; Kriewitz, C.R.; Hager, W.H.; Boes, R.M. An Experimental Investigation on Louvres and Angled Bar Racks. *J. Hydraul. Res.* **2018**, *56*, 59–75. [CrossRef]
47. Raynal, S.; Chatellier, L.; David, L.; Courret, D.; Larinier, M. Numerical Simulations of Fish-Friendly Angled Trashracks at Model and Real Scale. In Proceedings of the 35th IAHR World Congress, Chengdu, China, 8–13 September 2013.
48. Chatellier, L.; Wang, R.-W.; David, L.; Courret, D.; Larinier, M. Experimental Characterization of the Flow across Fish-Friendly Angled Trashrack Models. In Proceedings of the 34th IAHR World Congress, Brisbane, Australia, 26 June–1 July 2011; pp. 2776–2783.
49. Åkerstedt, H.O.; Eller, S.; Lundström, T.S. Numerical Investigation of Turbulent Flow through Rectangular and Biconvex Shaped Trash Racks. *Engineering* **2017**, *09*, 412–426. [CrossRef]
50. Leuch, C.; Beck, C.; Albayrak, I.; Vetsch, D.F.; Boes, R.M. Analysis and Optimization of Hydraulic Characteristics at Fish Guidance Structures Using CFD. In Proceedings of the 39th IAHR World Congress, Granada, Spain, 19–24 June 2022; pp. 3721–3728.
51. Pope, S.B. *Turbulent Flows*; Cambridge University Press: Cambridge, MA, USA; New York, NY, USA, 2000; ISBN 978-0-521-59125-6.
52. Keylock, C.J.; Hardy, R.J.; Parsons, D.R.; Ferguson, R.I.; Lane, S.N.; Richards, K.S. The Theoretical Foundations and Potential for Large-Eddy Simulation (LES) in Fluvial Geomorphic and Sedimentological Research. *Earth-Sci. Rev.* **2005**, *71*, 271–304. [CrossRef]
53. Rodi, W. Turbulence Modeling and Simulation in Hydraulics: A Historical Review. *J. Hydraul. Eng.* **2017**, *143*, 03117001. [CrossRef]
54. Nascimento, L.P.; Silva, J.B.C.; Di Giunta, V. Damage of Hydroelectric Power Plant Trash-Racks Due to Fluid-Dynamic Exciting Frequencies. *Lat. Am. J. Solids Struct.* **2006**, *3*, 223–243.
55. Ghamry, H.; Katopodis, C. Numerical Investigation of Turbulent Flow through Bar Racks in Closed Conduits. In Proceedings of the 9th International Symposium on Ecohydraulics, Vienna, Austria, 17–21 September 2012.
56. Paul, S.S.; Adaramola, M.S. Analysis of Turbulent Flow Past Bar-Racks. In Proceedings of the ASME 2014 International Mechanical Engineering Congress and Exposition, Montreal, QC, Canada, 14–20 November 2014.
57. Jeethulakshmi, G.; Sumam, K.S.; Sajikumar, N. Simulation of Head Loss in Trashrack—A Comparative Study. In Proceedings of the Flotek.g 2017—"Innovative Solutions in Flow Measurement and Control—Oil, Water and Gas", Palakkad, Kerala, India, 28 August 2017.
58. Čarija, Z.; Lučin, I.; Lučin, B.; Grbčić, L. Investigation of Numerical Simulation Parameters on Fluid Flow Around Trash-Racks. In Proceedings of the 29th DAAAM International Symposium, Vienna, Austria, 24–27 October 2018; Katalinic, B., Ed.; DAAAM International Vienna: Vienna, Austria, 2018; pp. 1046–1052, ISBN 978-3-902734-20-4.
59. Zhao, W.; Huhe, A. Large-Eddy Simulation of Three-Dimensional Turbulent Flow around a Circular Pier. *J. Hydrodyn.* **2006**, *18*, 765–772. [CrossRef]
60. Krajnović, S. Large Eddy Simulation of Flows around Ground Vehicles and Other Bluff Bodies. *Phil. Trans. R. Soc. A.* **2009**, *367*, 2917–2930. [CrossRef] [PubMed]
61. Gousseau, P.; Blocken, B.; Van Heijst, G.J.F. Quality Assessment of Large-Eddy Simulation of Wind Flow around a High-Rise Building: Validation and Solution Verification. *Comput. Fluids* **2013**, *79*, 120–133. [CrossRef]
62. Zdravkovich, M.M. *Flow around Circular Cylinders, Volume 1: Fundamentals*; Oxford Science Publications; Oxford University Press: Oxford, UK; New York, NY, USA, 1997.
63. Derakhshandeh, J.F.; Alam, M.M. A Review of Bluff Body Wakes. *Ocean Eng.* **2019**, *182*, 475–488. [CrossRef]
64. Khan, N.B.; Ibrahim, Z.; Bin Mohamad Badry, A.B.; Jameel, M.; Javed, M.F. Numerical Investigation of Flow around Cylinder at Reynolds Number = 3900 with Large Eddy Simulation Technique: Effect of Spanwise Length and Mesh Resolution. *Proc. Inst. Mech. Eng. Part M J. Eng. Marit. Environ.* **2019**, *233*, 417–427. [CrossRef]
65. Norberg, C. *Effect of Reynolds Number and a Low-Intensity Freestream Turbulence on the Flow around a Circular Cylinder*; Publikation Nr 87/2; Chalmers University of Technology, Department of Applied Thermodynamics and Fluid Mechanics: Gothenburg, Sweden, 1987.
66. Beaudan, P.; Moin, P. *Numerical Experiments on the Flow Past a Circular Cylinder at Sub-Critical Reynolds Number*; Report No. TF-62; Department of Mechanical Engineering, Stanford University: Stanford, CA, USA, 1994.
67. Williamson, C.H.K. Vortex Dynamics in the Cylinder Wake. *Annu. Rev. Fluid Mech.* **1996**, *28*, 477–539. [CrossRef]
68. Ong, L.; Wallace, J. The Velocity Field of the Turbulent Very near Wake of a Circular Cylinder. *Exp. Fluids* **1996**, *20*, 441–453. [CrossRef]

69. Kravchenko, A.G.; Moin, P. Numerical Studies of Flow over a Circular Cylinder at ReD = 3900. *Phys. Fluids* **2000**, *12*, 403–417. [CrossRef]
70. Franke, J.; Frank, W. Large Eddy Simulation of the Flow Past a Circular Cylinder at ReD = 3900. *J. Wind. Eng. Ind. Aerodyn.* **2002**, *90*, 1191–1206. [CrossRef]
71. Parnaudeau, P.; Carlier, J.; Heitz, D.; Lamballais, E. Experimental and Numerical Studies of the Flow over a Circular Cylinder at Reynolds Number 3900. *Phys. Fluids* **2008**, *20*, 085101. [CrossRef]
72. Lysenko, D.A.; Ertesvåg, I.S.; Rian, K.E. Large-Eddy Simulation of the Flow Over a Circular Cylinder at Reynolds Number 3900 Using the OpenFOAM Toolbox. *Flow Turbul. Combust* **2012**, *89*, 491–518. [CrossRef]
73. Ma, X.; Karamanos, G.-S.; Karniadakis, G.E. Dynamics and Low-Dimensionality of a Turbulent near Wake. *J. Fluid Mech.* **2000**, *410*, 29–65. [CrossRef]
74. Dong, S.; Karniadakis, G.E.; Ekmekci, A.; Rockwell, D. A Combined Direct Numerical Simulation–Particle Image Velocimetry Study of the Turbulent near Wake. *J. Fluid Mech.* **2006**, *569*, 185. [CrossRef]
75. Wissink, J.G.; Rodi, W. Numerical Study of the near Wake of a Circular Cylinder. *Int. J. Heat Fluid Flow* **2008**, *29*, 1060–1070. [CrossRef]
76. Xu, C.; Chen, L.; Lu, X. Large-Eddy and Detached-Eddy Simulations of the Separated Flow around a Circular Cylinder. *J. Hydrodyn.* **2007**, *19*, 559–563. [CrossRef]
77. D'Alessandro, V.; Montelpare, S.; Ricci, R. Detached–Eddy Simulations of the Flow over a Cylinder at Re = 3900 Using OpenFOAM. *Comput. Fluids* **2016**, *136*, 152–169. [CrossRef]
78. Young, M.E.; Ooi, A. Comparative Assessment of LES and URANS for Flow Over a Cylinder at a Reynolds Number of 3900. In Proceedings of the 16th Australasian Fluid Mechanics Conference, Crown Plaza, Gold Coast, Australia, 2–7 December 2007.
79. Deng, G.B.; Piquet, J.; Queutey, P.; Visonneau, M. Vortex-Shedding Flow Predictions with Eddy-Viscosity Models. In *Engineering Turbulence Modelling and Experiments*; Elsevier: Amsterdam, The Netherlands, 1993; pp. 143–152. ISBN 978-0-444-89802-9.
80. Rodi, W. Comparison of LES and RANS Calculations of the Flow around Bluff Bodies. *J. Wind. Eng. Ind. Aerodyn.* **1997**, *69–71*, 55–75. [CrossRef]
81. Lei, C.; Cheng, L.; Kavanagh, K. Spanwise Length Effects on Three-Dimensional Modelling of Flow over a Circular Cylinder. *Comput. Methods Appl. Mech. Eng.* **2001**, *190*, 2909–2923. [CrossRef]
82. Shao, J.; Zhang, C. Numerical Analysis of the Flow around a Circular Cylinder Using RANS and LES. *Int. J. Comput. Fluid Dyn.* **2006**, *20*, 301–307. [CrossRef]
83. Sumner, D. Two Circular Cylinders in Cross-Flow: A Review. *J. Fluids Struct.* **2010**, *26*, 849–899. [CrossRef]
84. Zhou, Y.; Mahbub Alam, M. Wake of Two Interacting Circular Cylinders: A Review. *Int. J. Heat Fluid Flow* **2016**, *62*, 510–537. [CrossRef]
85. Afgan, I.; Kahil, Y.; Benhamadouche, S.; Sagaut, P. Large Eddy Simulation of the Flow around Single and Two Side-by-Side Cylinders at Subcritical Reynolds Numbers. *Phys. Fluids* **2011**, *23*, 075101. [CrossRef]
86. Nguyen, Q.D.; Lu, W.; Chan, L.; Ooi, A.; Lei, C. A State-of-the-Art Review of Flows Past Confined Circular Cylinders. *Phys. Fluids* **2023**, *35*, 071301. [CrossRef]
87. Zovatto, L.; Pedrizzetti, G. Flow about a Circular Cylinder between Parallel Walls. *J. Fluid Mech.* **2001**, *440*, 1–25. [CrossRef]
88. Nguyen, Q.D.; Lei, C. Hydrodynamic Characteristics of a Confined Circular Cylinder in Cross-Flows. *Ocean Eng.* **2021**, *221*, 108567. [CrossRef]
89. Jiang, H.; Cheng, L. Large-Eddy Simulation of Flow Past a Circular Cylinder for Reynolds Numbers 400 to 3900. *Phys. Fluids* **2021**, *33*, 034119. [CrossRef]
90. Norberg, C. An Experimental Investigation of the Flow around a Circular Cylinder: Influence of Aspect Ratio. *J. Fluid Mech.* **1994**, *258*, 287–316. [CrossRef]
91. Ooi, A.; Lu, W.; Chan, L.; Cao, Y.; Leontini, J.; Skvortsov, A. Turbulent Flow over a Cylinder Confined in a Channel at Re = 3900. *Int. J. Heat Fluid Flow* **2022**, *96*, 108982. [CrossRef]
92. Celik, I.B.; Cehreli, Z.N.; Yavuz, I. Index of Resolution Quality for Large Eddy Simulations. *J. Fluids Eng.* **2005**, *127*, 949–958. [CrossRef]
93. Smagorinsky, J. General Circulation Experiments with the Primitive Equations: Part I. The Basic Experiment. *Mon. Wea. Rev.* **1963**, *91*, 99–164. [CrossRef]
94. ANSYS, Inc. *ANSYS Fluent Theory Guide*; Release 19.2; Southpointe: Canonsburg, PA, USA, 2018.
95. Menter, F.R. Two-Equation Eddy-Viscosity Turbulence Models for Engineering Applications. *AIAA J.* **1994**, *32*, 1598–1605. [CrossRef]
96. Idel'chik, I.E.; Ginevskiĭ, A.S. *Handbook of Hydraulic Resistance*, 4th ed. rev. and augmented; Begell House: Redding, CT, USA, 2007; ISBN 978-1-56700-251-5.
97. Gabl, R.; Gems, B.; Birkner, F.; Hofer, B.; Aufleger, M. Adaptation of an Existing Intake Structure Caused by Increased Sediment Level. *Water* **2018**, *10*, 1066. [CrossRef]
98. White, F.M. *Fluid Mechanics*, 6th ed.; Mcgraw-Hill Series in Mechanical Engineering; McGraw-Hill: New York, NY, USA, 2009; ISBN 978-0-07-352934-9.
99. Aigner, D.; Bollrich, G. *Handbuch der Hydraulik: Für Wasserbau und Wasserwirtschaft*, 1st ed.; Wissen Bauwesen; Beuth Verlag GmbH: Berlin, Germany; Vienna, Austria; Zürich, Seitzerland, 2015; ISBN 978-3-410-21346-8. (In German)

100. Lu, W.; Aljubaili, D.; Zahtila, T.; Chan, L.; Ooi, A. Asymmetric Wakes in Flows Past Circular Cylinders Confined in Channels. *J. Fluid Mech.* **2023**, *958*, A8. [CrossRef]
101. ANSYS, Inc. *ANSYS Fluent User's Guide*; Release 19.2; Southpointe: Canonsburg, PA, USA, 2018.
102. Wieselsberger, C. Neuere Feststellungen über die Gesetze des Flüssigkeits- und Luftwiderstandes. *Phys. Z.* **1921**, *22*, 321–328. (In German)
103. Blevins, R.D. *Applied Fluid Dynamics Handbook*; Van Nostrand Reinhold Co.: New York, NY, USA, 1984; ISBN 978-0-442-21296-4.
104. Singh, S.P.; Mittal, S. Flow Past a Cylinder: Shear Layer Instability and Drag Crisis. *Int. J. Numer. Meth. Fluids* **2005**, *47*, 75–98. [CrossRef]
105. Karabelas, S.J.; Koumroglou, B.C.; Argyropoulos, C.D.; Markatos, N.C. High Reynolds Number Turbulent Flow Past a Rotating Cylinder. *Appl. Math. Model.* **2012**, *36*, 379–398. [CrossRef]
106. Wen, P.; Qiu, W. Investigation of Drag Crisis Phenomenon Using CFD Methods. *Appl. Ocean. Res.* **2017**, *67*, 306–321. [CrossRef]
107. Lekkala, M.R.; Latheef, M.; Jung, J.H.; Coraddu, A.; Zhu, H.; Srinil, N.; Lee, B.-H.; Kim, D.K. Recent Advances in Understanding the Flow over Bluff Bodies with Different Geometries at Moderate Reynolds Numbers. *Ocean Eng.* **2022**, *261*, 111611. [CrossRef]
108. Naudascher, E.; Rockwell, D. *Flow-Induced Vibrations: An Engineering Guide*; Dover Publications: Mineola, NY, USA, 2005; ISBN 978-0-486-44282-2.
109. Kim, D.-H.; Yang, K.-S.; Senda, M. Large Eddy Simulation of Turbulent Flow Past a Square Cylinder Confined in a Channel. *Comput. Fluids* **2004**, *33*, 81–96. [CrossRef]
110. Bai, H.; Alam, M.M. Dependence of Square Cylinder Wake on Reynolds Number. *Phys. Fluids* **2018**, *30*, 015102. [CrossRef]
111. Davis, R.W.; Moore, E.F.; Purtell, L.P. A Numerical-Experimental Study of Confined Flow around Rectangular Cylinders. *Phys. Fluids* **1984**, *27*, 46. [CrossRef]
112. Alam, M.M.; Zhou, Y.; Wang, X.W. The Wake of Two Side-by-Side Square Cylinders. *J. Fluid Mech.* **2011**, *669*, 432–471. [CrossRef]
113. Zhao, F.; Wang, R.; Zhu, H.; Ping, H.; Bao, Y.; Zhou, D.; Cao, Y.; Cui, H. Large-Eddy Simulations of Flow Past a Circular Cylinder near a Free Surface. *Phys. Fluids* **2021**, *33*, 115108. [CrossRef]
114. Cao, Y.; Tamura, T. Large-Eddy Simulations of Flow Past a Square Cylinder Using Structured and Unstructured Grids. *Comput. Fluids* **2016**, *137*, 36–54. [CrossRef]
115. Lemkecher, F.; Chatellier, L.; Courret, D.; David, L. Contribution of Different Elements of Inclined Trash Racks to Head Losses Modeling. *Water* **2020**, *12*, 966. [CrossRef]
116. Feigenwinter, L.; Vetsch, D.; Kammerer, S.; Kriewitz, C.; Boes, R. Conceptual Approach for Positioning of Fish Guidance Structures Using CFD and Expert Knowledge. *Sustainability* **2019**, *11*, 1646. [CrossRef]
117. Maddahi, M.; Hagenbüchli, R.; Mendez, R.; Zaugg, C.; Boes, R.M.; Albayrak, I. Field Investigation of Hydraulics and Fish Guidance Efficiency of a Horizontal Bar Rack-Bypass System. *Water* **2022**, *14*, 776. [CrossRef]
118. Zöschg, H.; Dobler, W.; Aufleger, M.; Zeiringer, B. Evaluation of Hydraulics and Downstream Fish Migration at Run-of-River Hydropower Plants with Horizontal Bar Rack Bypass Systems by Using CFD. *Water* **2023**, *15*, 1042. [CrossRef]
119. Zhao, M.; Cheng, L.; Zhou, T. Direct Numerical Simulation of Three-Dimensional Flow Past a Yawed Circular Cylinder of Infinite Length. *J. Fluids Struct.* **2009**, *25*, 831–847. [CrossRef]
120. Liang, H.; Duan, R.-Q. Effect of Lateral End Plates on Flow Crossing a Yawed Circular Cylinder. *Appl. Sci.* **2019**, *9*, 1590. [CrossRef]
121. Zhou, B.; Wang, J.; Jin, G.; Zhou, Y.; Wang, X.; Gho, W.M. Large Eddy Simulation of Flow Past an Inclined Finite Cylinder. *Ocean. Eng.* **2022**, *258*, 111504. [CrossRef]
122. Kriewitz-Byun, C.R. *Leitrechen an Fischabstiegsanlagen: Hydraulik und fischbiologische Effizienz*; ETH Zurich: Zurich, Switzerland, 2015. (In German) [CrossRef]
123. Albayrak, I.; Boes, R.M. Fish Guidance Structure with Wide Bar Spacing: Mechanical Behavioural Barrier. In *Novel Developments for Sustainable Hydropower*; Rutschmann, P., Kampa, E., Wolter, C., Albayrak, I., David, L., Stoltz, U., Schletterer, M., Eds.; Springer International Publishing: Cham, Switzerland, 2022; pp. 99–104, ISBN 978-3-030-99137-1.
124. Heller, V. Scale Effects in Physical Hydraulic Engineering Models. *J. Hydraul. Res.* **2011**, *49*, 293–306. [CrossRef]
125. Haug, J.; Brinkmeier, B.; Tutzer, R.; Aufleger, M. Hybride Barrieren zur Optimierung von Stabrechen zum Fischschutz. *Wasserwirtsch* **2021**, *111*, 48–53. (In German) [CrossRef]
126. Khan, L.A.; Wicklein, E.A.; Rashid, M.; Ebner, L.L.; Richards, N.A. Computational Fluid Dynamics Modeling of Turbine Intake Hydraulics at a Hydropower Plant. *J. Hydraul. Res.* **2004**, *42*, 61–69. [CrossRef]
127. Waldy, M.; Gabl, R.; Seibl, J.; Aufleger, M. Alternative Methoden für die Implementierung von Rechenverlusten in die 3D-numerische Berechnung mit FLOW-3D. *Österr. Wasser-Abfallw.* **2015**, *67*, 64–69. (In German) [CrossRef]
128. Özbey, C.; Kucukali, S. A Numerical Investigation of Hydrodynamics of Fish-Friendly Fine Screens. In Proceedings of the 40th IAHR World Congress, Vienna, Austria, 21–25 August 2023; pp. 1935–1944. [CrossRef]
129. Wagner, F.; Keuneke, R.; Kampa, E.; Kemper, M.; Naumann, S. *Forum Fischschutz und Fischabstieg: Ergebnisse und Ausblick*; Umweltbundesamt: Dessau-Roßlau, Germany, 2023; p. 52. (In German)

Disclaimer/Publisher's Note: The statements, opinions and data contained in all publications are solely those of the individual author(s) and contributor(s) and not of MDPI and/or the editor(s). MDPI and/or the editor(s) disclaim responsibility for any injury to people or property resulting from any ideas, methods, instructions or products referred to in the content.